



HAL
open science

Petrogenesis and $^{40}\text{Ar}/^{39}\text{Ar}$ dating of hydrothermal romanechite from the sub-aerial fault-related Romanèche Mn deposit (France)

Augustin Dekoninck, Gilles Ruffet, Julien Baptiste, Robert Wyns, Simon Philippo, Yishen Zhang, Olivier Namur

► **To cite this version:**

Augustin Dekoninck, Gilles Ruffet, Julien Baptiste, Robert Wyns, Simon Philippo, et al.. Petrogenesis and $^{40}\text{Ar}/^{39}\text{Ar}$ dating of hydrothermal romanechite from the sub-aerial fault-related Romanèche Mn deposit (France). *Chemical Geology*, 2023, 618, pp.121280. 10.1016/j.chemgeo.2022.121280 . insu-03917908

HAL Id: insu-03917908

<https://insu.hal.science/insu-03917908>

Submitted on 2 Jan 2023

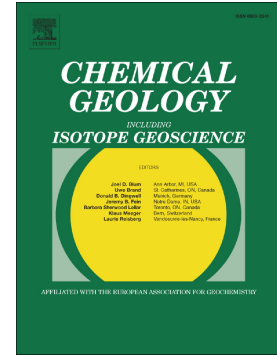
HAL is a multi-disciplinary open access archive for the deposit and dissemination of scientific research documents, whether they are published or not. The documents may come from teaching and research institutions in France or abroad, or from public or private research centers.

L'archive ouverte pluridisciplinaire **HAL**, est destinée au dépôt et à la diffusion de documents scientifiques de niveau recherche, publiés ou non, émanant des établissements d'enseignement et de recherche français ou étrangers, des laboratoires publics ou privés.

Journal Pre-proof

Petrogenesis and $^{40}\text{Ar}/^{39}\text{Ar}$ dating of hydrothermal romanechite from the sub-aerial fault-related Romanèche Mn deposit (France)

Augustin Dekoninck, Gilles Ruffet, Julien Baptiste, Robert Wyns, Simon Philippo, Yishen Zhang, Olivier Namur



PII: S0009-2541(22)00574-5

DOI: <https://doi.org/10.1016/j.chemgeo.2022.121280>

Reference: CHEMGE 121280

To appear in: *Chemical Geology*

Received date: 10 August 2022

Revised date: 29 November 2022

Accepted date: 21 December 2022

Please cite this article as: A. Dekoninck, G. Ruffet, J. Baptiste, et al., Petrogenesis and $^{40}\text{Ar}/^{39}\text{Ar}$ dating of hydrothermal romanechite from the sub-aerial fault-related Romanèche Mn deposit (France), *Chemical Geology* (2022), <https://doi.org/10.1016/j.chemgeo.2022.121280>

This is a PDF file of an article that has undergone enhancements after acceptance, such as the addition of a cover page and metadata, and formatting for readability, but it is not yet the definitive version of record. This version will undergo additional copyediting, typesetting and review before it is published in its final form, but we are providing this version to give early visibility of the article. Please note that, during the production process, errors may be discovered which could affect the content, and all legal disclaimers that apply to the journal pertain.

© 2022 Published by Elsevier B.V.

Petrogenesis and $^{40}\text{Ar}/^{39}\text{Ar}$ dating of hydrothermal romanechite from the sub-aerial fault-related Romanèche Mn deposit (France).

Augustin DEKONINCK^{1,*}, Gilles RUFFET^{2,3}, Julien BAPTISTE⁴, Robert WYNS⁴, Simon PHILIPPO⁵, Yishen ZHANG⁶, Olivier NAMUR⁶

¹Institute of Life-Earth-Environment (ILEE), University of Namur, 61 rue de Bruxelles B-5000, Namur, Belgium. augustin.dekoninck@unamur.be

²CNRS (CNRS/INSU) UMR 6118, Géosciences Rennes, F-35042 Rennes Cedex, France. gilles.ruffet@univ-rennes1.fr

³Université de Rennes 1, Géosciences Rennes, 35042 Rennes France. gilles.ruffet@univ-rennes1.fr

⁴BRGM (French Geological Survey), DGR/GAT, 1, Av. Cl. Guillemin, BP 36009, 45060 Orléans Cedex 2, France. j.baptiste@brgm.fr, r.wyns@brgm.fr

⁵Laboratoire de Minéralogie, Musée National d'Histoire Naturelle, Rue Münster 25, 2160 Luxembourg, Luxembourg. simon.philippo@mnh.lu

Department of Earth and Environmental Sciences, KU Leuven, Celestijnlaan 200e – Box 2408, B-3001, Leuven, Belgium. yishen.zhang@kuleuven.be, olivier.namur@kuleuven.be

Abstract

This study discusses the hydrothermal formation of romanechite ($\text{Ba}_{0.7}\text{Mn}_{4.5}\text{O}_{10.1.1}\text{H}_2\text{O}$) in the Romanèche Mn deposit and the significance of its age by combining ore petrogenesis and $^{40}\text{Ar}/^{39}\text{Ar}$ ages. Romanechite occurs as a minor phase in various manganese deposit types and remains poorly studied in comparison with other K-bearing Mn oxides (i.e., coronadite group) because of its scarcity, small grain size, intermixing and poor crystallinity. The fault-controlled Romanèche Mn deposit (Massif Central, Eastern France) investigated herein exhibits a well-crystallized and late stage massive romanechite ore occurring in a quartz-barite-fluorite gangue. Petrographical and geochemical data support manganese ore formation under sub-aerial conditions with temperatures close to fluorite precipitation (100-200°C) and characterized by a Mn-Ba-W-As association. Five out of the eight studied samples have produced $^{40}\text{Ar}/^{39}\text{Ar}$ plateau ages ranging from 25.2 ± 0.3 to 18.2 ± 0.5 Ma. Despite a low K content (0.1-0.6 wt.% K), the good crystallinity of romanechite due to its epithermal formation likely favours a better production and/or retention of the radiogenic argon than poorly crystallized phases of supergene origin. Therefore, the dataset identifies a period of at least c. 7.6 My of discontinuous hydrothermal activity, which is consistent with graben-related fault reactivation and likely volcanic activity in the Massif Central. Ultimately, this study confirms the feasibility of romanechite $^{40}\text{Ar}/^{39}\text{Ar}$ dating.

Keywords: romanechite, manganese, $^{40}\text{Ar}/^{39}\text{Ar}$ dating, epithermal mineralization, Mn oxide

1. Introduction

Assessing the age of mineral deposition is a key issue to understand the timescales of formation of mineral resources. When datable minerals are present, it is of great importance to identify the process by which they have precipitated in order to better constrain the ore genesis. Mn oxides have long been used to date supergene deposits due to the extensive occurrence of K-bearing Mn oxides (e.g., Ruffet et al., 1996; Li et al., 2007; Beauvais and Chardon, 2013; Vasconcelos et al., 2013; Deng et al., 2016; Vasconcelos and Carmo, 2018; Jean et al., 2019; Dekoninck et al., 2019, 2021; De Putter and Ruffet, 2020). The most common species belong to the coronadite group $[(\text{Ba}^{2+}, \text{Pb}^{2+}, \text{Sr}^{2+}, \text{Na}^+, \text{K}^+)(\text{Mn}^{4+} \text{Mn}^{3+} \text{ or } ^{2+})_8\text{O}_{16}]$ (Lippolt and Hautmann, 1995; Ruffet et al., 1996; Vasconcelos et al., 1995, 1994, 1992) forming a typical tunnel. The tunnel Mn oxides are built of chains of edge-sharing MnO_6 octahedra, and the chains share corners to produce frameworks that have tunnels with square or rectangular cross sections (Post, 1999). The 2X2 tunnel crystallographic structure of coronadite allows a good retentivity of the $^{40}\text{Ar}^*$ produced by the decay of radioactive structural ^{40}K , hence providing a remarkable tool for $^{40}\text{Ar}/^{39}\text{Ar}$ dating. Far less known, romanechite $[\text{Ba}_{0.66} \text{Mn}^{4+}_{3.68} \text{Mn}^{3+}_{1.32} \text{O}_{10} \cdot 1.37 \text{H}_2\text{O}]$ or $(\text{Ba}, \text{H}_2\text{O})_2(\text{Mn}^{3+}, \text{Mn}^{4+})_5\text{O}_{10}$ (Post, 1999; Turner and Post, 1988) is also suitable for $^{40}\text{Ar}/^{39}\text{Ar}$ geochronology (Vasconcelos, 1999) as it can host structural K in the 2X3 tunnel structure (Burns and Burns, 1979; Post, 1999).

Although the majority of Mn oxides precipitate under supergene conditions, many deposits host Mn oxides directly formed from hydrothermal solutions (Choubert and Faure-Muret, 1973; Conly et al., 2011; Lacroix et al., 2010; Dekoninck et al., 2018; Glasby et al., 2005; Hewett, 1964; Leal et al., 2008; Liakopoulos et al., 2001; O'Reilly, 1992; Papavassiliou et al., 2017; Roy, 1981, 1968). The Mn oxide ore precipitates on top of the hydrothermal system by mixing of ascending hydrothermal fluids with descending oxygenated meteoric water (Hewett, 1964; Roy, 1968, 1981). These sub-surface hypogene ores are composed of higher valence oxides such as romanechite, coronadite group minerals, pyrolusite and ramsdellite. Whereas discriminating between Mn oxides formed under supergene versus epithermal conditions is relatively simple in active systems, it remains challenging in ancient ore systems (i.e. Gossans).

The Romanèche manganese deposit (Saône-et-Loire department, France)(Fig. 1) is predominantly composed of romanechite (type-locality mineral; Lacroix, 1910) located atop

a vein-type mineralization (Fig. 2; Bouladon, 1958). The Mn oxide ore is trapped in and aside the boundary fault-zone separating the Massif Central (MC) Variscan granitic basement and the Bresse graben filled by Mesozoic and Cenozoic sediments (Figs. 1 and 2). The mineralization has long been considered as a supergene gossan capping an underlying and hidden hydrothermal mineralization (Dolomieu, 1796; Drouot, 1857; Hautmann and Lippolt, 2000; Lacroix, 1910; Lougnon, 1981) due to the predominance of tetravalent Mn oxides. However, Bouladon (1958) was the first to argue for an hydrothermal formation of the romanèchite stage. Therefore, the Romanèche deposit can be useful to discuss the hydrothermal versus supergene formation of Mn oxides on top of vein-type mineralization.

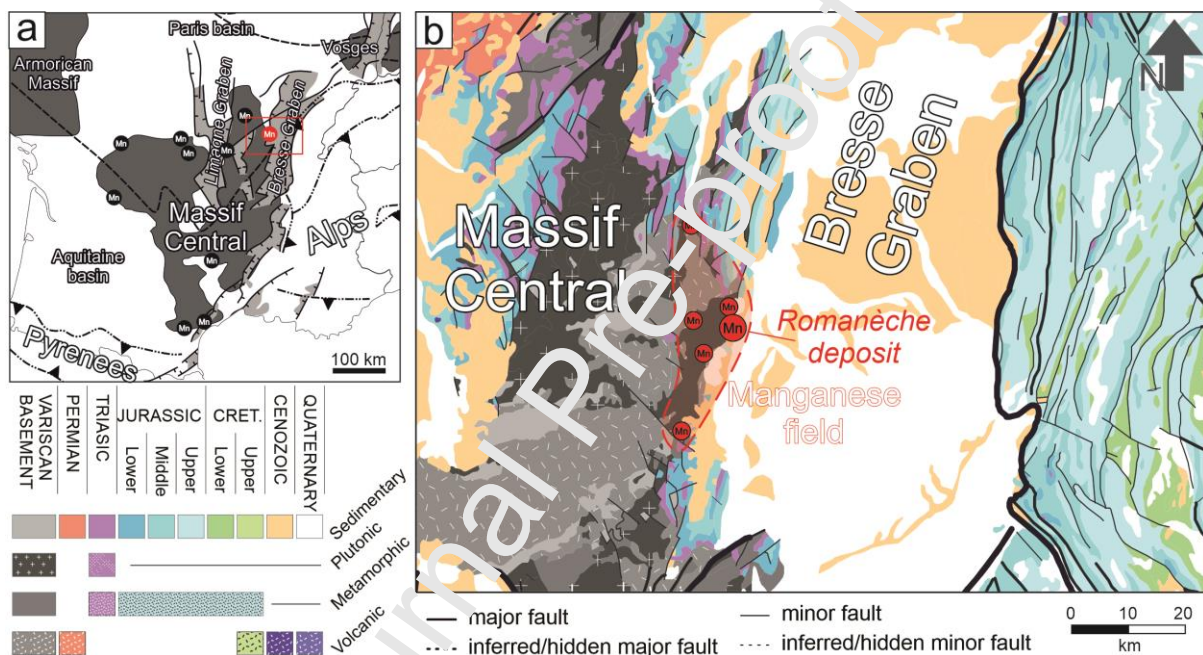


Fig. 1. Geological situation of the Romanèche Mn deposit and surrounding Mn mineralization. **a.** Location of the Romanèche deposit among other Mn occurrences of the French Massif Central. **b.** Geological map of the Romanèche Mn(-F) manganese field between the Massif Central and the Bresse Graben (modified after Chantraine et al., 2003).

Hautmann and Lippolt (2000) were the first, as part of a global Central European study of Mn-oxides, to conduct a geochronological analysis of this deposit in order to discuss weathering processes in Western Europe. Our study provides a more detailed analysis of the composition, ore genesis and timing of the Romanèche manganese deposit by combining X-ray diffraction (XRD), scanning electron microscope with energy-dispersive spectroscopy (SEM-EDX), electron probe micro-analysis (EPMA), whole rock geochemistry and $^{40}\text{Ar}/^{39}\text{Ar}$ dating of romanèchite. This dataset is used to refine the formation process of romanèchite and

to provide new ages in order to better understand the formation of the Romanèche deposits and other similar deposits worldwide.

2. Hydrothermal Mn oxide deposits

Hydrothermal Mn deposits are known worldwide. They all have low tonnage and reserves (e.g., Ouarzazate Mn field, Morocco; Cape Vani, Greece; SW, USA; Choubert and Faure-Muret, 1973; Conly et al., 2011; Decrée et al., 2010; Dekoninck et al., 2018; Glasby et al., 2005; Hewett, 1964; Holtstam and Mansfeld, 2001; Leal et al., 2008; Liakopoulos et al., 2001; O'Reilly, 1992; Papavassiliou et al., 2017; Roy, 1981, 1968). These deposits are fault-controlled and occur as veins that may be up to 1.5 m thick, extend horizontally up to 500 m and be traced to depths of up to 150 m. The vertical extension is rarely beyond 1 km (Hewett, 1964). The Mn oxide ore precipitates in the upper part of the hydrothermal system, showing an increasing gradation of higher valence oxides, including the Mn⁴⁺-Mn³⁺-bearing romanéchite, coronadite group minerals, pyrolusite and ramsdellite (Hewett, 1964; Roy, 1981, 1968). They show high concentrations of Ba, As, W, Sr, Be, Sb, Tl and Ge. They are consistently accompanied by barite, fluorite, quartz and carbonates as gangue minerals. Silicification is the most common form of wall-rock alteration near the main Mn vein (Hewett, 1964). Sericitization is also reported. Barite and fluorite precipitation can either predate or postdate the Mn oxides. Anhydrosiderite is found in some places and is a proof of hydrothermalism (Hewett, 1964). Below the high-valence Mn oxide ore, the deeper ore includes Mn²⁺-bearing minerals such as carbonates, silicate and oxides (Fusswinkel et al., 2013; Hewett, 1966; Madondo et al., 2020).

3. Mineralization style

The Romanèche manganese deposit is associated to the major fault-zone separating the Variscan granitic basement of the MC and the Triassic-Jurassic cover of the Bresse Graben. The Mn ore follows this structure over an NNE striking length of c. 750 m (Figs. 1b and 2). This fault has an offset of ~650 meters and has been active several times since the Variscan orogenesis (Bouladon, 1958). The Romanèche deposit is no longer accessible; the numerous galleries have been closed by the regional authorities. The main access has been sealed by a concrete cap behind the Romanèche church and the other wells obstructed since the eighties. Therefore, the today's Mn ore consists of mining wastes reused in some walls of the village or disseminated in the surrounding vineyards (see Appendix A). The only direct observations of the ore are minor Mn veins hosted in granites. Several Mn occurrences outcrop over a

greater area with fluorite and barite (Drouot, 1857), which defines a larger manganese field of 10x35 km² following the major fault direction (Fig. 1b). The Mn deposit consists of (i) two parallel lodes (“Grand filon” and “Petit filon”) with a N35°E direction and dip angles of 50-75°SE hosted in Carboniferous granites (“Petit filon”) or in the fault zone (“Grand filon”) and (ii) a stratabound epigenetic mineralization replacing the Sinemurian limestone (Fig. 2; Lacroix, 1910; Bouladon, 1958). Both mineralization styles are reworked in the alluvium cover. The Romanèche ore combines romanechite with fluorite, quartz and barite. Three major ore facies can be observed: (1) Mn crust (Fig. 3a), (2) Massive Mn ore (with or without fluorite; Fig. 3b), (3) Mn breccia (Fig. 3c). Hematite is also present in little amounts but becomes abundant at depth with barite (Bouladon, 1958, Lacroix, 1910) and locally arseniosiderite $\text{Ca}_2\text{Fe}_3\text{O}_2(\text{AsO}_4)_3 \cdot 3\text{H}_2\text{O}$ (type-locality mineral, Du rénoy, 1842).

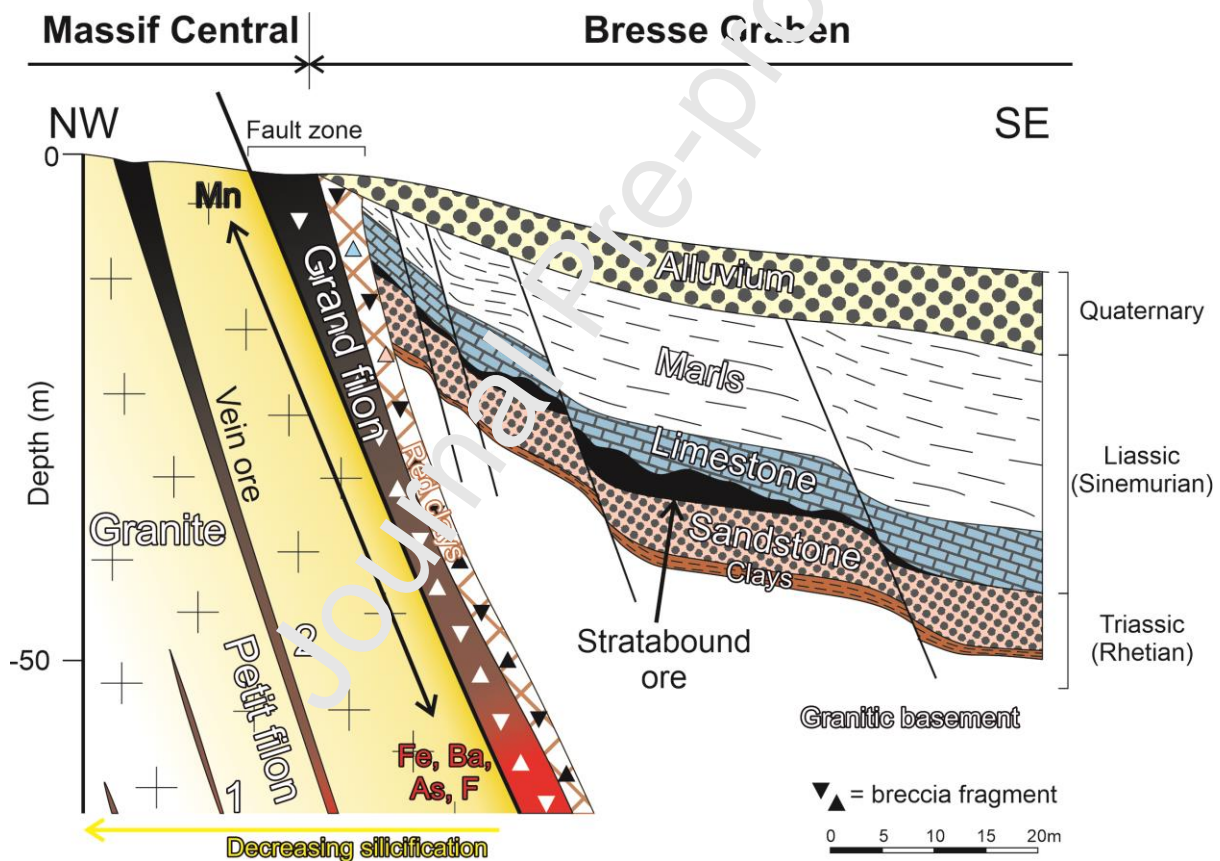


Fig. 2. N125°E cross-section through the Romanèche deposit (Bouladon, 1958).

4. Materials and methods

Forty-four samples have been collected in the field. Most of them come from mining wastes in vineyards and village walls around the main historical mining wells (see Appendix A for details and photographs). One sample is from the collection of the Museum National d’Histoires Naturelles du Luxembourg. The initial location of these samples is unknown but

they likely come from the most important past extraction sites. The mineralogy of 32 samples of these samples was determined by X-ray diffraction. Sixteen samples were further selected and examined in detail by optical and scanning electron microscopy on polished sections. EPMA analyses has been carried on romanechite to obtain quantitative chemical analyses of major and minor elements. This mineralogical and petrographical determination was complemented by geochemical analyses of major and trace elements on 14 whole rock samples. Based on these results, we selected eight samples for $^{40}\text{Ar}/^{39}\text{Ar}$ geochronology.

4.1 Mineralogical and petrographical analysis

Polished sections (16) were prepared for petrographic analyses at the Geomaterial Preparation Laboratory of the University of Namur (Belgium). XRD analyses of powdered samples were performed using an X-ray Panalytical X'Pert Pro diffractometer and a PHILLIPS PW3710 (CuK α radiation) of the PC2 platform (University of Namur), operating at 40 kV and 30 mA. The main mineral phases were identified using the ICDD View software with PDF-2 database (Powder Diffraction File 2019). Polished sections were studied by optical microscopy and electron microscopy using a JEOL 6010 LV and a JSM 7500-F SEM coupled with an ULTRA MINI-COMP Energy Dispersive Spectrometer (EDS) hosted at the Microscopy Service of the University of Namur. Four polished sections have also been observed and analyzed with a JEOL JXA-8530F EPMA equipped with a high brightness Schottky field emission electron gun (FEG), at the Department of Materials Engineering of KU Leuven (Leuven, Belgium). The following primary standards were used for K α calibration: Mn metal (Mn), quartz (Si), almandine garnet (Al), barite (Ba), skutterudite (As, Co), hematite (Fe), plagioclase-An65 (Na), biotite (Mg), anhydrite (Ca), galena (Pb), celestite (Sr), sphalerite (Zn), tungsten metal (WO $_3$) and cuprite (Cu). Details about standards, accuracy, precision and analytical conditions are given in Appendix A – Supplementary Material. The water content is calculated using charge base structural formulae (Table 1).

Table 1. EPMA analysis of romanechite in the Romanèche Mn deposit.

Lab	N	Si	Al	B	M	As	F	N	M	C	K	P	S	Z	W	C	C	H	T
el	o.	O ₂	O ₃	O	O ₂	O ₅	O	O ₂	O	O	O ₂	O	O	O	O ₃	O	O	O ₂	O _{total}
19R		0.	0.	1	7	0.	0.	0.	0.	0.	0.	0.	0.	0.	2.	0.	0.	4.	10
OM	0	1	51	6.	5.	45	0	02	05	1	0	0	2	0	10	0	0	8	0.

15		4		4	5		9			3	3	0	4	1		5	4	4	67
				5	3														
19R		0.		1	7		0.			0.	0.	0.	0.	0.		0.	0.	4.	10
OM		0	0.	6	5.		0	0.	0.	1	0	0	1	0	2.	2	0	7	0.
15	1	3	46	7	8	30	8	08	00	5	2	1	6	0	61	0	4	8	98
19R		0.		1	7		0.			0.	0.	0.	0.	0.		0.	0.	4.	10
OM		0	0.	6	1	0.	1	0.	0.	2	0	0	2	0	3.	0	0	7	0.
15	6	8	43	2	5	33	3	31	00	2	5	0	3	0	01	5	0	1	30
19R		0.		1	7		0.			0.	0	0.	0.	0.		0.	0.	4.	99
OM		0	0.	7	0	0.	0	0.	0.	1	0	0	3	0	2.	0	0	7	.8
15	7	0	41	2	7	68	9	11	03	8	2	0	4	2	23	8	2	9	0
19R		0.		1	7		0.			0.	0.	0.	0.	0.		0.	0.	4.	99
OM		0	0.	5	1	0.	0	0.	0.	1	0	0	2	0	2.	0	0	7	.6
15	8	0	45	0	2	13	5	02	06	5	2	1	9	0	06	3	7	4	7
19R		0.		1	7		0.			0.	0.	0.	0.	0.		0.	0.	4.	99
OM		0	0.	2	9	0.	0	0.	0.	1	0	0	2	0	1.	0	0	8	.8
15	9	3	51	1	8	65	9	02	03	3	5	0	6	0	99	5	6	1	6
19R		0.		1	7		0.			0.	0.	0.	0.	0.		0.	0.	4.	10
OM		0	0.	8	8	0.	1	0.	0.	0	0	0	2	0	1.	0	0	8	0.
15	10	0	47	2	0	46	1	03	03	8	1	0	0	0	74	0	9	1	65
19R		0.		1	7		0.			0.	0.	0.	0.	0.		0.	0.	4.	10
OM		0	0.	7	1	0.	0	0.	0.	1	0	0	2	0	2.	0	0	9	2.
15	11	8	51	3	6	34	5	07	01	2	1	0	0	0	18	5	4	2	48
19R		0.		1	7		0.			0.	0.	0.	0.	0.		0.	0.	4.	10
OM		1	0.	6	7.	0.	0	0.	0.	0	0	0	1	0	2.	0	0	9	2.
15	12	6	51	5	5	09	7	05	02	8	2	0	4	0	40	4	0	9	72

				7	8														
19R		0.		6.	6.		0.			0.	0.	0.	0.	0.		0.	0.	4.	10
OM		0	0.	1	9	0.	1	0.	0.	1	0	0	1	0	2.	0	0	9	1.
15	13	8	44	0	3	36	0	09	00	3	2	0	7	0	32	4	1	5	72
19R		0.		6.	5.		0.			0.	0.	0.	0.	0.		0.	0.	4.	10
OM		0	0.	3	8	0.	1	0.	0.	1	0	0	2	0	2.	0	0	8	0.
15	14	1	48	7	0	56	2	03	04	5	3	0	7	0	05	7	6	5	87
19R		0.		6.	6.		0.			0.	0.	0.	0	0.		0.	0.	4.	10
OM		0	0.	3	1	0.	0	0.	0.	1	0	0	3	0	2.	0	0	8	1.
15	15	0	47	8	6	47	6	09	00	0	3	0	2	0	06	7	1	3	05
19R		0.		6.	6.		0.			0.	0.	0.	0.	0.		0.	0.	4.	10
OM		0	0.	5	2	0.	5	0	0.	1	0	0	1	0	2.	1	0	8	1.
15	5	3	53	8	7	06	0	05	08	3	2	1	2	0	12	0	4	9	53
19R		0.		6.	4.		0.			0.	0.	0.	0.	0.		0.	0.	4.	99
OM		0	0.	3	9	0	0	0.	0.	1	0	0	1	0	1.	1	0	7	.7
15	4	0	53	4	2	09	8	08	00	4	2	6	5	0	93	2	0	6	2
19R		0.		6.	7.		1.			0.	0.	0.	0.	0.		0.	0.	4.	10
OM		0	0.	4	0	0.	0	0.	0.	1	0	0	1	0	1.	1	0	8	2.
15	3	5	48	3	3	21	0	18	02	9	6	8	5	0	97	1	5	8	90
19R		0.		6.	5.		1.			0.	0.	0.	0.	0.		0.	0.	4.	10
OM		0	0.	2	1	0.	2	0.	0.	1	0	1	1	0	1.	0	0	8	0.
15	2	0	29	7	1	03	5	02	00	4	4	3	6	0	73	9	9	3	16
19R		0.		6.	3.		0.			1.	0.	0.	1.	0.		0.	0.	4.	99
OM		0	0.	9	2	0.	5	0.	0.	4	2	0	0	0	0.	0	0	0	.0
32a	16	1	49	3	7	06	5	01	00	8	5	0	0	0	96	1	1	1	4

OM		2	42	4.	6.	55	5	31	01	9	2	0	6	0	04	0	0	5	.4
32a		9		4	3		2			2	6	3	8	0		4	1	3	0
				7	3														
19R		0.		1	7		0.			0.	0.	0.	0.	0.		0.	0.	4.	10
OM		0	0.	3	7	0.	1	0.	0.	2	0	0	3	0	0.	0	0	9	1.
32a	26	0	45	7	0	66	1	10	00	5	6	0	0	0	00	0	4	1	94
19R		0.		1	7		0.			0.	0.	0.	0.	0.		0.	0.	5.	10
OM		1	0.	9	6	0.	1	0.	0.	0	0	0	1	0	0.	0	0	0	3.
32a	27	2	47	5	9	41	0	00	02	7	5	0	7	4	13	0	0	6	28
19R		0.		1	7		0.			0.	0.	0.	0.	0.		0.	0.	4.	99
OM		0	0.	7	6	1.	0	0.	0.	5	0	0	2	0	0.	0	0	7	.9
32a	28	0	47	5	6	02	7	18	00	1	7	0	9	3	11	3	2	2	2
19R		0.		1	7		0.			0.	0.	0.	0.	0.		0.	0.	4.	10
OM		0	0.	8	8	0.	2	0.	0.	5	0	0	1	0	0.	0	0	8	3.
32a	34	0	51	2	8	21	3	12	10	5	7	0	9	1	58	0	2	1	09
19R		0.		1	8		0.			0.	0.	0.	0.	0.		0.	0.	4.	10
OM		0	0.	9	0	0.	3	0.	0.	7	1	0	1	0	0.	0	0	8	4.
32a	35	3	47	0	8	28	3	17	07	4	0	0	8	1	69	0	0	3	88
19R		0.		1	7		0.			0.	0.	0.	0.	0.		0.	0.	4.	10
OM		3	0.	2	8	0.	3	0.	0.	3	1	0	1	0	1.	0	0	8	1.
32a	36	8	50	4	1	56	6	14	00	5	0	4	4	0	13	0	0	4	60
19R		0.		1	7		0.			0.	0.	0.	0.	0.		0.	0.	4.	10
OM		1	0.	6	3	0.	0	0.	0.	6	3	0	6	0	0.	0	0	8	0.
32a	42	2	40	9	7	75	9	23	03	4	1	0	3	3	51	1	2	6	71
	m	0.	0.	1	8	1.	1.	0.	0.	1.	0.	0.	1.	0.	3.	0.	0.	5.	10
	ax	3	54	6.	0.	02	2	31	10	4	3	1	0	0	01	2	0	0	4.

l		d				, Q			He	Ro	Q,	Ro	,	Ro	Q,	,	
			Gr ani te (wt .)	Gn eis s	Gr ani te	M n ore	M n ore	M n ore	M n- Fe ore	M n ore	M n ore	M n ore	M n ore	M n- Fe ore	M n ore	M n ore	
F	%	01	F U S- IS E		<	0.0	0.0	0.0	0.1	0.0	14.5	34.6	16.4	6.4	2.7	42.2	
S O ₄	%	05	S O P	<	<	<	<	<	<	0.0	18.4	0.4	0.0	0.0	0.5	<	
Si O ₂	%	01	F U S- IC P	69.92	74.19	71.06	3.4	6	9	11.28	89.1	24.94	5.73	0.4	38.85	3.92	0.64
Al ₂ O ₃	%	01	F U S- IC P	14.28	14.63	13.39	0.87	1.48	1.68	1.02	1.67	0.59	0.11	0.14	0.34	1.48	0.16
Fe ₂ O ₃	%	01	F U S- IC P	1.89	0.81	0.26	0.97	0.41	0.79	15.96	0.63	<	0.0	1.48	0.38	12.83	0.33
Mn	%	00	F U	0.035	0.015	0.019	46.03	56.59	58.9	43.34	5.16	0.028	12.24	43.09	17.61	54.79	7.418

O			S- IC P															
MgO	0.01%	0.01	FUS- IC P	0.95	0.54	0.56	0.21	0.14	0.11	0.06	0.03	0.04	0.02	0.02	0.04	0.13	0.02	
CaO	0.01%	0.01	FUS- IC P	0.67	0.51	0.25	12.47	0.20	0.41	0.67	0.25	0.17	52.84	25.06	10.03	4.83	63.58	
Na ₂ O	0.01%	0.01	FUS- IC P	2.39	4.76	0.66	0.16	0.26	0.04	0.07	0.06	0.01	0.02	0.04	0.04	0.05	0.02	
K ₂ O	0.01%	0.01	FUS- IC P	5.75	2.12	9.95	0.47	0.33	0.34	0.69	1.04	0.22	0.05	0.99	0.15	0.46	0.06	
TiO ₂	0.00%	0.00	FUS- IC P	0.417	0.212	0.219	0.043	0.037	0.039	0.032	0.021	0.018	0.003	0.003	0.001	0.044	0.005	
P ₂ O ₅	0.01%	0.01	FUS- IC P	0.25	0.21	0.16	0.08	0.02	0.16	0.04	0.03	0.05	0.04	0.03	0.02	0.03	0.01	< 0.01

L OI	%		G R A V	2.6 9	1.4 7	0.8 9	17. 35	10. 14	11. 06	9.1	1.2 1	6.3 1	5.8 1	7.9 2	8.3 2	11. 79	2.4 1
L OI 2	%		F U S- IC P	2.7 5	1.5 6	1.0 5	17. 36	10. 14	11. 06	9.1 1	1.2 1	6.3 3	5.8 1	7.9 2	8.3 2	11. 79	2.4 1
To tal	%	0 . 0 1	F U S- IC P	99. 83	10 0.2	98. 83	82. 01	75. 62	76. 11	82 28	99 16	56. 51	78. 35	78. 62	88. 25	78. 3	74. 65
To tal 2	%	0 . 0 1	F U S- IC P	99. 89	10 0.3	98. 99	82. 01	75. 62	76. 11	82. 28	99. 16	56. 5	78. 36	78. 62	88. 25	78. 3	74. 65
Fe ₂ O ₃ (T)	%	0 . 0 1	F U S- IC P	2.5 5	1.6 9	1.8 2	0.9 8	0.4 3	0.8	15. 97	0.6 4	0.1 8	1.4 9	0.3 9	12. 84	0.8 2	0.3 4

Table 2. Continued.

A na ly te S y m bo	U n it	.	D L h o d	A na ly sis M et h o d	19 R O M 12	19 R O M 17	19 R O M 43	19 R O M 09	19 R O M 15	19 ro m2 0c	19 ro m2 1a	19 ro m2 1e	19 R O M 26	19 R O M 29	19 ro m3 2a	19 ro m3 2b	19 R O M 33	19 R O M 37
							Ca, Ro , Q	Ro , Q	Ro , Q	Ro , He	Qz , Ro	F, Ba, Q,	F, Q, Ro ,	F, Ro , F, Ro	Q, F, Ro Q,	Ro , Q,	F, Ro ,	

	m		S-M S														
C u	p p m	1 0	F U S-M S	20	10	20	10	64 0	13 0	14 0	20	< 10	50	70	30	80	40
Z n	p p m	3 0	F U S-M S	40	< 30	< 30	22 0	30	20 0	33 0	< 30	< 30	40	50	16 0	16 0	< 30
G a	p p m	1	F U S-M S	29	23	23	15	35	21	38	16	1	6	19	24	30	4
G e	p p m	1	F U S-M S	2	2		41	11 0	38	69	6	1	11	34	57	41	5
A s	p p m	5	F U S-M S	43	48	17	35 50	25 20	22 70	67 60	26 4	16	14 50	20 40	34 50	20 90	89 4
R b	p p m	2	F U S-M S	27 8	10 0	37 9	46	16	26	48	49	21	4	24	13	33	5

			M														
			S														
S	p		F														
n	m	1	U														
			S-														
			M														
			S	9	8	5	<1	<1	1	1	1	<1	<1	1	1	<1	<1
			F														
			U														
S	p	0	S-														
b	m	5	M					11	38.	16	10.			34.	94.	35.	37.
			S	1.7	1.7	1.4	11	9	7	8	4	4.5	30	7	6	5	4
			F														
			U														
C	p	0	S-														
s	m	5	M		15.												
			S	30	4	4.4	9	18.	11.								
			F														
			U														
B	p		S-				95	14	14	97	10	24	33	81	39	13	15
a	m	2	IC	12	52	69	19	36	03	38	84	83	16	26	98	03	61
			P	18	7	1	0	00	00	0	0	00	0	0	0	00	0
			F														
			U														
L	p	0	S-														
a	m	1	M	23.	22.	12.	21.	27.		24.			15.	13.	14.	12.	
			S	2	2	5	2	8	9.8	8	4.1	5.2	7	9	4	4	9.5
			F														
			U														
C	p	0	S-														
e	m	1	M	84.	52.		18.	23.	14.	40.			17.	12.	32.		
			S	8	3	27	4	3	4	9	8.2	8	2	3	2	11	9.1
Pr	p	0	F	5.6	6.6	2.9	4.1	5.8	2.2	4.1	0.9	1.0	2.7	2.2	3	2.1	1.7

	p	.	U	6	6	3		6	8	4	8	5	5	1		1	1
	m	0	S-														
		5	M														
			S														
N	p	0	F														
d	p	.	U														
	m	1	S-	21.		10.		23.	10.	14.		10.		10.			
			S	5	28	4	16	4	4	1	3.8	4.8	1	8.6	6	9	6.4
S	p	0	F														
m	p	.	U														
	m	1	S-														
			S	4.2	7.4	2.5	2.7	5.2	2.8	2.7	0.8	2.1	2.4	1.8	2.3	1.9	1.4
E	p	0	F														
u	p	.	U														
	m	5	S-	0.8	1.0	0.5	<	<	<			<		<		<	
			M	9	4	9	0.6	0.0	0.0	0.8	0.1	0.0	0.8	0.0	0.9	0.0	0.2
			S	5	4	9	5	5	7	3	5	2	5	2	5	7	7
G	p	0	F														
d	p	.	U														
	m	1	S-														
			S	3.5	7.5	2.1	2.7	4	3.2	2.6	0.6	2.8	2.7	1.9	2.6	2.1	1.4
T	p	0	F														
b	p	.	U														
	m	1	S-														
			S	0.6	1.2	0.3	0.4	0.5	0.4	0.4	0.1	0.5	0.4	0.3	0.4	0.3	0.2
D	p	0	F														
y	p	.	U														
	m	1	S-														
			M	3	7.1	1.9	2.1	2.2	2.2	2.2	0.5	3.3	2.3	1.7	2.2	1.6	1.3

	m	1	S-														
			M														
			S														
W	p	1	F														
	p		U														
	p		S-														
	m	1	M														
			S	19	15	20	17	20	31	20	15		83	16	10	24	10
								0	40	10	0	5	9	70	00	10	30
TI	p	0	F														
	p	.	U														
	m	1	S-														
			M				26	30.	10	57.			22.	17	32.	75.	21.
			S	3.3	1.2	2	9	1	5	7	43	0.1	4	2	8	1	9
P	p		F														
	p		U														
	m	5	S-														
			M														
			S	29	8	34	8	7	21	9	17	30	91	34	0	30	7
Bi	p	0	F														
	p	.	U														
	m	4	S-														
			M														
			S	<	<	<	<	11.	<	<	<	<	<	<	<	<	<
				0.4	0.4	0.4	0.4	6	0.4	0.4	0.4	0.4	0.4	0.4	0.4	0.4	0.4
T	p	0	F														
	p	.	U														
	m	1	S-														
			M	21.		15.											
			S	5	8.5	2	1.1	0.4	1.5	2.1	1.5	1.6	0.2	0.1	0.5	1.3	0.3
U	p	0	F														
	p	.	U														
	m	1	S-														
			M				21.		35.	36.			23.	49.	20.	56.	14.
			S	5.2	1.9	4.2	8	3.4	1	2	5.7	1.3	2	8	9	1	9

Fe		0	TI														
O	%	1	T R	0.6	0.8	1.4	<	<	<	<	<	0.2	<	<	<	<	<

4.3 $^{40}\text{Ar}/^{39}\text{Ar}$ K-Mn oxides geochronology

The eight romanechite sub-samples selected for geochronology were hand-picked from crushed rocks, washed in distilled water in an ultrasonic bath, and dried to avoid dust adsorbed on surface grains. Several grains have been taken for each sub-sample. The crystallinity, purity and composition were checked by XRD on aliquots (see Research data). The reflexion line at $\sim 3.10\text{\AA}$ on XRD pattern was used to identify the presence of coronadite group minerals and/or pyrolusite. In addition, each grain was investigated by SEM to control the degree of purity. Grains containing inclusions of minerals were discarded from the selection. Based on XRD and SEM analysis, we were able to select eight grains of pure romanechite and of sufficient size (3 to 7 μm) to ensure high bulk potassium (see SEM view of the selected grains in Appendix A). Four samples (15, ROM05, 13, 20b and 23) have been duplicated to compare the results. A total of 12 grains have been analysed from the 8 sub-samples. $^{40}\text{Ar}/^{39}\text{Ar}$ step-heating analyses were performed with a CO_2 laser probe coupled with a MAP 215 mass spectrometer, using the procedure described by Ruffet *et al.* (1991, 1995, 1996, 1997). Irradiation of samples was performed at McMaster Nuclear Reactor (Canada) in the 8C facility and lasted 50 h with a global efficiency (J/h) of $8.15 \times 10^{-5} \text{ h}^{-1}$. The irradiation standard was sanidine TCRs ($28.608 \pm 0.033 \text{ Ma}$; Renne *et al.*, 1998, 2010 and 2011). Blank analyses were performed routinely before the first and after three to four runs, and were subtracted from the subsequent sample gas fractions. Apparent age errors were plotted at the 1 σ level. These ages do not include errors on the $^{40}\text{Ar}^*/^{39}\text{Ar}_K$ ratio and age of the monitor and decay constants. Plateau ages were calculated only if 70% or more of the $^{39}\text{Ar}_K$ was released in at least three or more contiguous steps that yielded apparent ages within the 1 σ of the integrated age of the plateau segment. Pseudo-plateau ages were defined with the same criteria if the plateau-segment contained less than 70% of the $^{39}\text{Ar}_K$ released (Cheilletz *et al.*, 1999). The errors on the $^{40}\text{Ar}^*/^{39}\text{Ar}_K$ ratio and age of the monitor and decay constants were included in the final calculation of the errors of the (pseudo-) plateau ages. Analytical data and parameters used for calculations, such as isotopic ratios measured on pure K and Ca salts, mass discrimination, atmospheric argon ratios, J parameter, decay constants are in the electronic supplementary data material.

5. Results

5.1 Petrography, mineral chemistry and paragenetic sequence

The Mn ore is composed of romanechite with colloform texture (Fig. 3a) constituted by aggregates of micrometric needles (usually 10-1000 μm length) (Fig. 3d), dendrites (Fig. 3e), or tabular crystals (Fig. 3f). Most of the romanechite grows onto the gangue minerals and host granite breccia (Fig. 3c and 3g). Small voids often remain empty (Fig. 3g). Colloform romanechite displays growth bands of slightly variable compositions (Figs. 3d and g) attributed to variations in the amounts of Ba, W and H_2O . Two generations of romanechite are identified with crosscutting relations (Figs. 3h and i). The first generation (rmn-1) is Ca-rich, when rmn-2 has no particular geochemical feature. Romanechite is a vein-filling mineral, meaning that no replacement texture has been observed or described, i.e. by replacement of Mn-rich carbonates or silicates. Romanechite is ubiquitous but some samples contain small amounts of cryptomelane, coronadite and hollandite. These minerals occur as veinlets or as filling of remaining voids in romanechite (Fig. 3h). Pyrolusite is observed as tiny aggregates of bipyramidal laths within the romanechite matrix (Fig. 3j). Hematite is early with respect to romanechite (Fig. 3k).

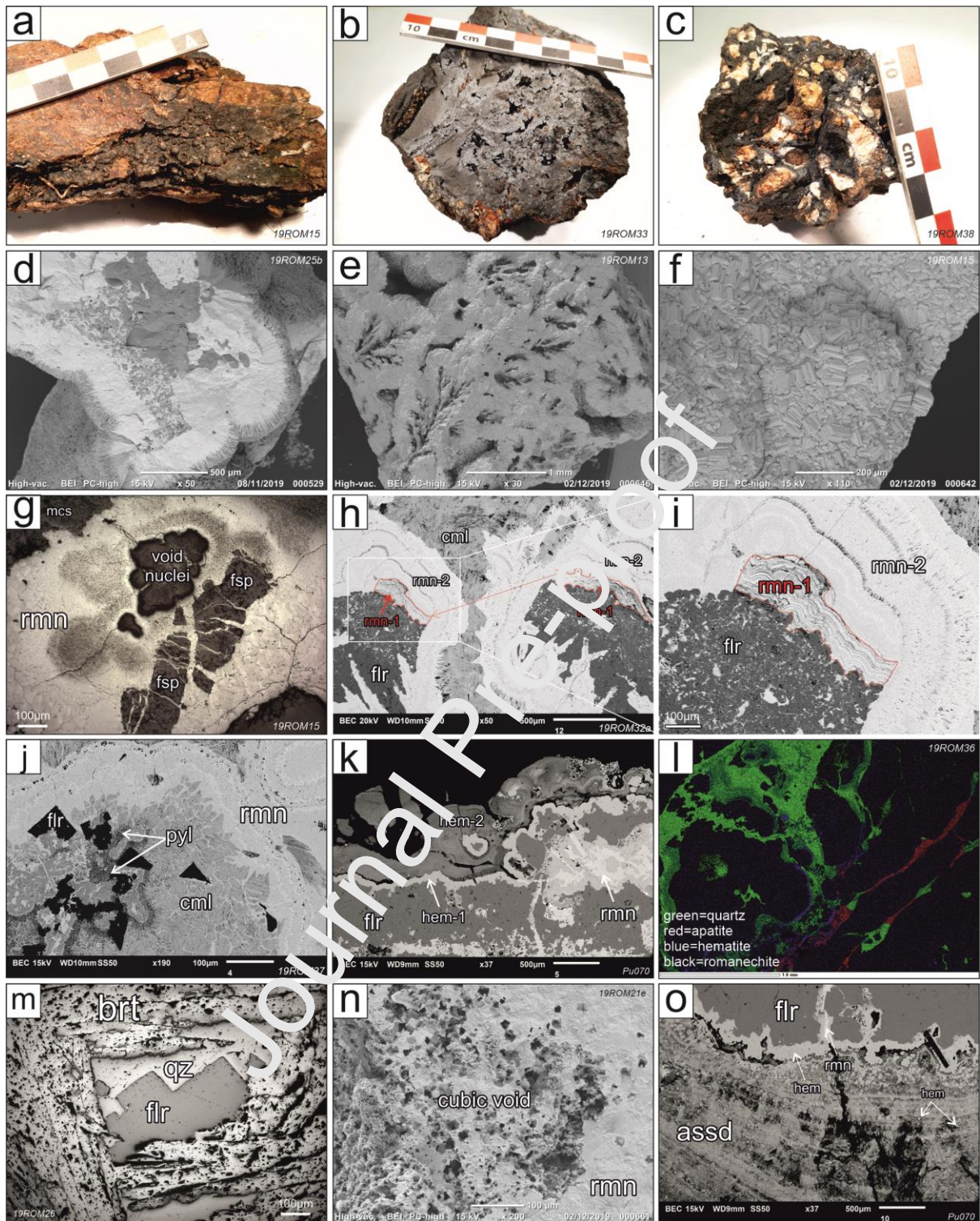


Fig. 3. Petrographic observation of the romanechite-rich ore of Romanèche. **a.** Hand specimen of Mn crust in the host granite at the Les Espagnes deposit. **b.** Hand specimen of the massive Mn ore from the Romanèche deposit. **c.** Hand specimen of the Mn ore breccia containing fragments of the host granite. **d.** Back-scattered electron (BSE) view of colloform romanechite around a quartz-fluorite nuclei. **e.** SEM-BSE view of typical dendrites of romanechite. **f.** SEM-BSE view of prismatic tabular crystals of romanechite (dated sample).

g. Cross-polarized view of romanechite surrounding feldspars and voids (fluorite?) under reflected light. **h.** SEM-BSE view of two colloform generations of romanechite: rmn-1 is brecciated and enclosed in rmn-2. Cryptomelane veinlets split the romanechite matrix into two parts. **i.** Close-up of Fig. 3e showing details of successive generations of romanechite growing onto the fluorite gangue. **j.** SEM-BSE view of pyrolusite between fluorite and romanechite-cryptomelane. **k.** SEM-BSE view of successive crystallization layers of hematite and its relation with gangue minerals and romanechite. **l.** Combined chemical maps of Si (green; quartz), P (red; apatite), Fe (blue; hematite) and Mn (black; romanechite) showing late veins of quartz and apatite. **m.** Cross-polarized view of barite, quartz and fluorite under reflected light. **n.** SEM-BSE view of romanechite hosting cubic voids of former fluorite. **o.** SEM-BSE view of arseniosiderite growing onto hematite and crosscutting relation with romanechite. rmn = romanechite, fsp = feldspar, cml = cryptomelane, flr = fluorite, pyl = pyrolusite, hem = hematite, brt = barite, assd = arseniosiderite.

Gangue minerals are predominantly quartz and fluorite. Barite is also frequent, whereas arseniosiderite $[\text{Ca}_2\text{Fe}_3(\text{AsO}_4)_3\text{O}_2 \cdot 3(\text{H}_2\text{O})]$ and apatite are relatively scarce. Several generations of quartz are observed: one is younger than romanechite, whereas the other postdates the Mn oxides in fractures with the apatite veins (Fig. 3l). Purple fluorite, when associated with Mn oxides, but colourless or green in unmineralized samples, forms typical cubic crystals (Figs. 3j and m). Fluorite grows onto barite laths prior to ore-forming minerals and quartz (Fig. 3m). Some authors identified fluorite crystals coating the second generation of quartz (Drouot, 1857), some of the fluorite coating romanechite (Chermette, 1975). In heavily mineralized samples, we suspect that some cubic voids (Fig. 3n) were initially fluorite ghosts. Arseniosiderite forms fibrous crystals growing onto hematite and is intersected by romanechite (Fig. 3o).

These petrographic observations show that barite, fluorite and quartz gangue minerals form early and successively in the paragenetic sequence (Figs. 3m and 4). The Fe stage occurs at depth with hematite and arseniosiderite. Romanechite is the highly dominant Mn oxide. Romanechite is late in the paragenetic sequence and likely coeval or younger to the fluorite stage: fluorite can either predate or postdate romanechite. In the latter case, this might be coeval with partial dissolution of the first fluorite generation. Pyrolusite and coronadite group minerals accompany the massive romanechite stage, forming the Mn ore. Apatite, barite and quartz have (re)crystallized later (Fig. 4).

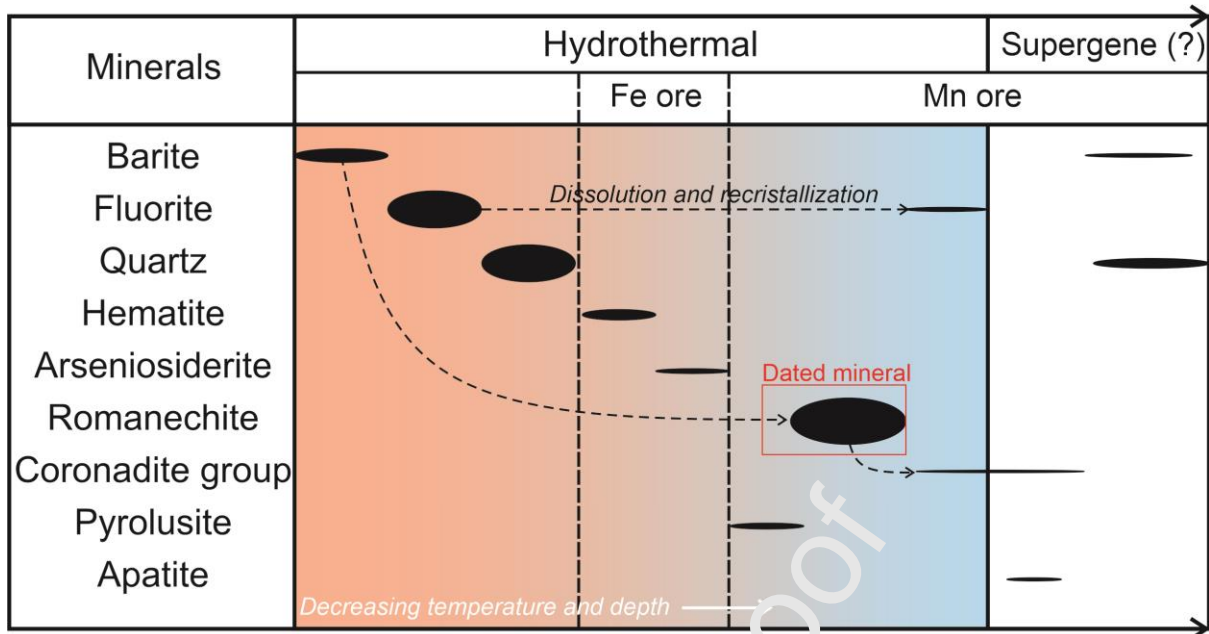


Fig. 4. Paragenetic sequence of the Romanèche Mn deposit based on petrographic observations and SEM analyses.

Crystallographic site occupancy has been determined according to Turner and Post (1988): high ionic radii cations (Ba, H₂O, K, Ca, Na, Sr) occupy the tunnel, when the others (As, W, Si, Al, Fe³⁺, Cu, Co, Pb, Zn) may substitute to Mn³⁺ in the [MnO₆] octahedra. We calculated structural formulae using the charge-base method with 20 neutralising charges in the theoretical formulae of romanechite $[\text{Ba}_{0.66}\text{Mn}^{4+}_{3.68}\text{Mn}^{3+}_{1.32}\text{O}_{10}\cdot 1.34\text{H}_2\text{O}]$. The amount of H₂O is deduced from the full tunnel site occupancy (=2) and averaged at 4.78 wt.% H₂O. The studied samples deviate from the theoretical formula of romanechite by high amounts of W (0-2.4 wt.% W) and As (0-0.7 wt.%). The amount of K is between 0.01 and 0.26 wt.% K. Finally, the average structural formulae of romanechite from 33 EPMA points is $[\text{Ba}_{0.54}\text{Ca}_{0.04}\text{Sr}_{0.02}\text{Na}_{0.02}\text{K}_{0.01}(\text{Mn}_{4.57}\text{W}_{0.03}\text{Al}_{0.05}\text{As}_{0.02}\text{Fe}_{0.02})\text{O}_{10}\cdot 1.37\text{H}_2\text{O}]$.

5.2 Whole rock geochemistry of the Mn(-F) ore

The host granite has a felsic composition with 69.9 to 74.2 wt.% SiO₂. This silica content is enhanced by silicification and weathering. The MnO concentration is low, ranging between 0.02 and 0.04 wt.%. The other major elements have variable concentrations. Arsenic (17-48 ppm As) and tungsten (15-20 ppm W) are relatively high in comparison with the Upper Continental Crust (Fig. 5a). Rare Earth Elements profiles normalized on the Upper Continental Crust are flat (Fig. 5b).

The major element contents of the Mn ore are MnO (0.03-58.9 wt.%), F (0-42.2 wt.%), CaO (0.2-63.6), SiO₂ (0.4-89.1 wt.%), Fe₂O₃ (0.3-16.0 wt.%) and Ba (1.1-24.8 wt.%). The low MnO value is due to high content of the gangue minerals. Some elements, usually considered as trace elements show high concentrations; W (5-13,200 ppm), As (16-6,760 ppm) and Sr (364-3,337 ppm Sr). Tungsten is hosted by romanechite (Table 1). The other metals are slightly enriched (Co, Cu, Zn; Table 2; Fig. 5a). Rare Earth Elements are not enriched (19.7-95.0 ppm REE) compared to the UCC, characterized by flat patterns with a slight negative Ce anomaly (Table 1; Fig. 5b).

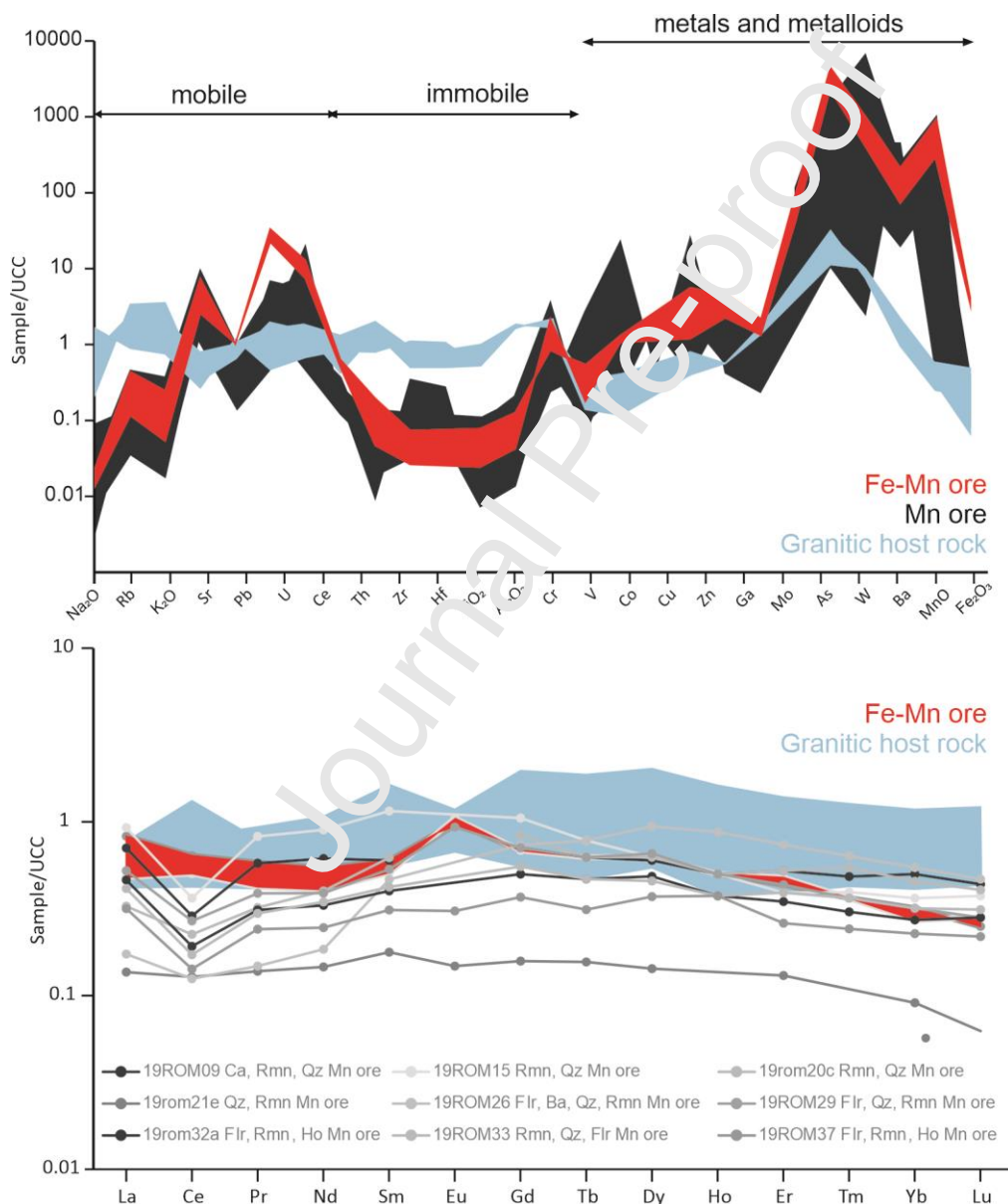


Fig. 5. Geochemistry of the Mn ore, Fe-Mn ore and host rocks compared to the Upper Continental Crust (UCC; McLennan, 2001). **a.** Trace element patterns of the romanechite-bearing Mn ore, Fe-Mn ore and granitic basement rocks in the Romanèche deposit. **b.** Rare

Earth Element patterns of the Mn ore, Fe-Mn ore and host rocks. Ca: calcite; Rmn: romanechite; Qz: quartz; Flr: fluorite; Brt: barite.

5.3 $^{40}\text{Ar}/^{39}\text{Ar}$ geochronology

$^{40}\text{Ar}/^{39}\text{Ar}$ analyses of romanechite provide ages spanning the period between late Chattian to Burdigalian (18.2-25.3 Ma; Fig. 6; Table 3).

$^{40}\text{Ar}/^{39}\text{Ar}$ age spectra (Fig. 6; Table 3) yields five plateau ages at 18.2 ± 0.5 Ma [19ROM30; 85.9% of total $^{39}\text{Ar}_K$ released and mean square of weighted deviates (MSWD)=0.26], 23.0 ± 0.4 Ma (19ROM05; 92.1% of total $^{39}\text{Ar}_K$ released and MSWD=0.74), 23.4 ± 0.5 Ma (19ROM20b; 86.2% of total $^{39}\text{Ar}_K$ released and MSWD=0.05), 23.5 ± 0.4 Ma (19ROM29; 84.3% of total $^{39}\text{Ar}_K$ released and MSWD=0.54) and 25.2 ± 0.3 Ma (19ROM21a; 94.3% of total $^{39}\text{Ar}_K$ released and MSWD=0.44) and a concordant pseudo-plateau age at 22.8 ± 0.3 Ma (61.2% of total $^{39}\text{Ar}_K$ released and MSWD=0.20) provided by duplicate experiment performed on sample 19ROM05. These plateau ages are validated by the processing in the inverse isochron diagrams (correlation diagram) ($^{36}\text{Ar}/^{40}\text{Ar}$ vs. $^{39}\text{Ar}_K/^{40}\text{Ar}^*$; Hanes et al., 1985; Roddick et al., 1980; Turner, 1971) with initial ratios ($^{40}\text{Ar}/^{36}\text{Ar}$)_i indistinguishable from the atmospheric ratio ($^{40}\text{Ar}/^{36}\text{Ar} = 295.56$ according to Lee et al. (2006)) and MSWDs in accordance with the statistical validity criteria. All these experiments provide rather flat $^{37}\text{Ar}_{Ca}/^{39}\text{Ar}_K$ (# Ca/K) spectra with ratios in the range 0.6–1.2. Note that the $^{37}\text{Ar}_{Ca}/^{39}\text{Ar}_K$ (# Ca/K) ratios calculated for romanechite are significantly higher than those usually observed for Mn oxides of the coronadite group (~0.1). These ages are consistent with those of Hautmann and Lippolt (2000) at 25.8 ± 0.4 , 24.9 ± 0.4 , 20.9 ± 0.7 and 20.8 ± 0.6 Ma.

Table 2 Summary of significant geochronological information and validated plateau ages (PA) and Isochron ages based on $^{40}\text{Ar}/^{39}\text{Ar}$ and $^{37}\text{Ar}_{Ca}/^{39}\text{Ar}_K$ spectra and Inverse isochron (correlation) diagrams ($^{36}\text{Ar}_{atm}/^{40}\text{Ar}_{atm}$ vs. $^{39}\text{Ar}_K/^{40}\text{Ar}^*$) of romanechite in the Romanèche deposit.

Label	Ore type	PA (Ma)	$\pm 1 \sigma$	Isochron age (Ma)	$\pm 1 \sigma$	($^{40}\text{Ar}/^{36}\text{Ar}$) _i	$\pm 1 \sigma$	Comments	Reference
RF4a1-k		20.9	0.73					Plateau	Hautmann and Lippolt (2000)
RF4a2		20.8	0.3					Plateau	Hautmann and

-k			6						Lippolt (2000)
RF4b-k		24.9	0.39					Plateau	Hautmann and Lippolt (2000)
RF1-k	Colloform	25.8	0.38					Plateau	Hautmann and Lippolt (2000)
19RO M05-1	Stockwork	22.8	0.3	22.7	2.7	296.3	1.72	Plateau	This study
19RO M05-2		23	0.5	23.2	0.6	297.5	2.9	Plateau	This study
19RO M13	Crust	-	-	-	-	-	-	Contamination by old material	This study
19RO M15	Crust	-	-	-	-	-	-	Contamination by old material	This study
19RO M20b-1	Massive	23.4	0.5	23.4	0.9	298.5	2.6	Plateau	This study
19RO M20b-2		-	-	-	-	-	-	Saddle, contamination	This study
19RO M21a	Stockwork	25.2	0.3	25.2	0.4	298.6	0.9	Plateau	This study
19RO M23	Stockwork	-	-	-	-	-	-	Saddle, contamination	This study
19RO M29	Breccia fragment	23.5	0.4	23.8	1.3	296.2	1.4	Plateau	This study
19RO M30	Massive	18.2	0.5	18.7	0.8	296.9	1.9	Staircase - Ca-rich	This study

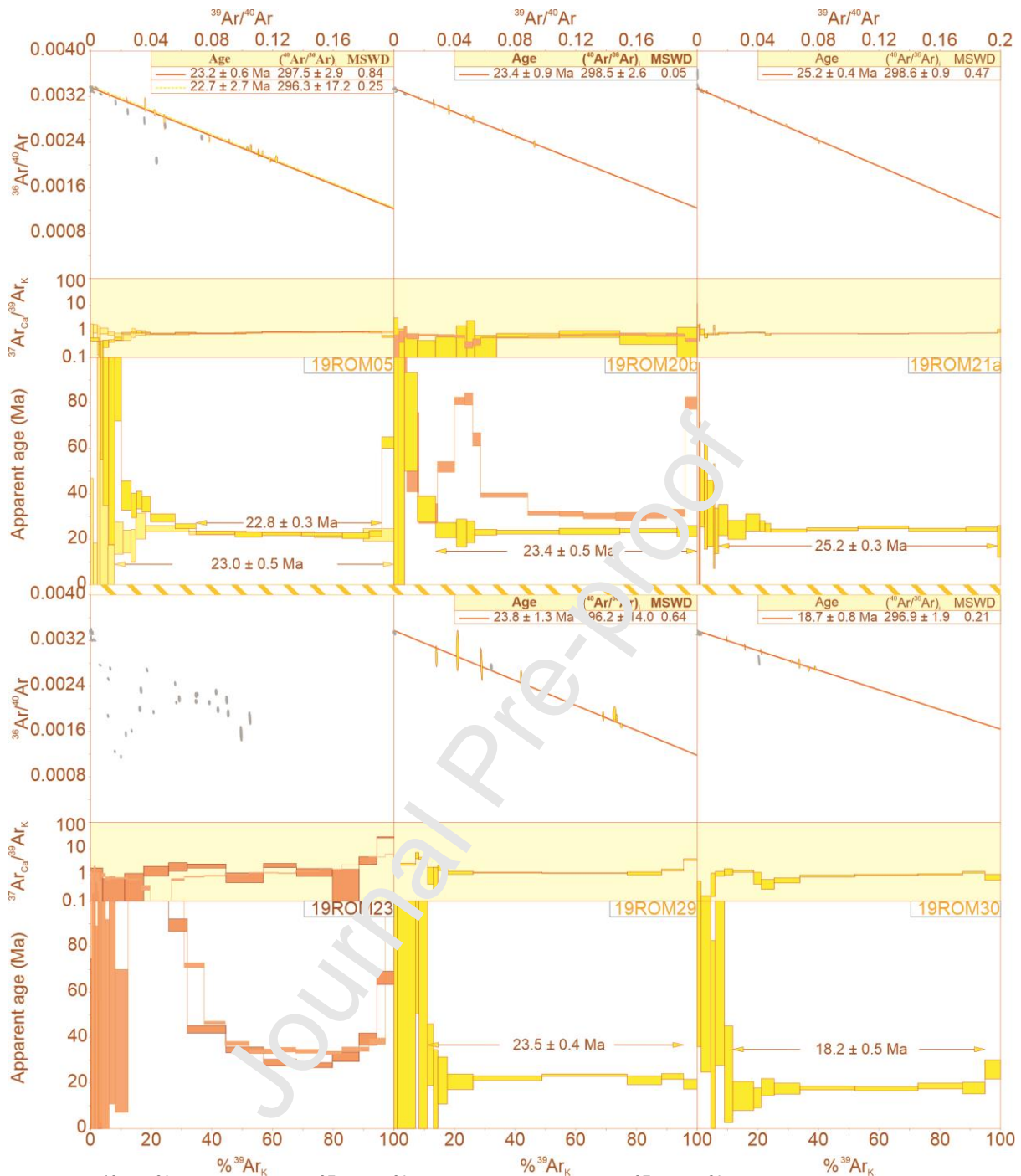


Fig. 6. $^{40}\text{Ar}/^{39}\text{Ar}$ age and $^{37}\text{Ar}_{\text{Ca}}/^{39}\text{Ar}_{\text{K}}$ (# Ca/K with $^{37}\text{Ar}_{\text{Ca}}/^{39}\text{Ar}_{\text{K}} = \text{CaO}/\text{K}_2\text{O} / 2.179$; (Deckart et al., 1997) spectra and inverse isochron ($^{36}\text{Ar}/^{40}\text{Ar}$ vs. $^{39}\text{Ar}/^{40}\text{Ar}$) diagrams of romanéchite samples 19ROM05, 20b, 21a, 23, 29 and 30 from Romanèche deposit. Detailed results are present in supplementary data. Apparent age error bars are at the 1σ level; errors in the J-parameter are not included. Plateau, pseudo-plateau and isochron ages are given with 1σ uncertainties and include errors in the J-parameter. Grey ellipses are excluded from isochron regression, MSWD stands for Mean Squares of Weighted Deviates.

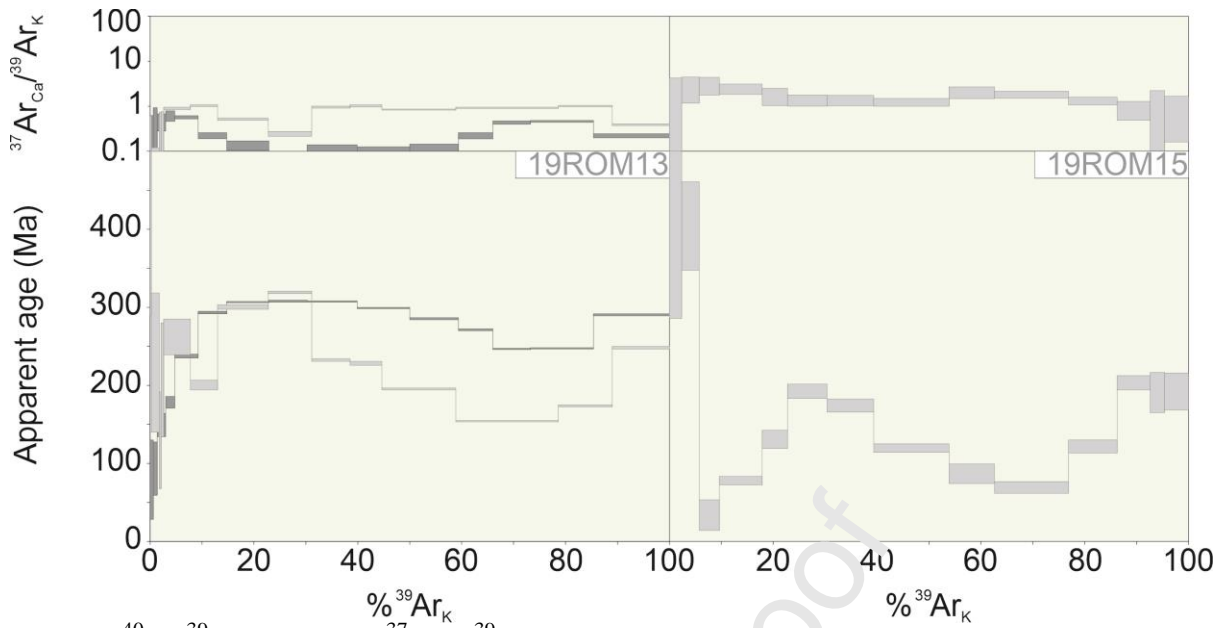


Fig. 7. $^{40}\text{Ar}/^{39}\text{Ar}$ age and $^{37}\text{Ar}_{\text{Ca}}/^{39}\text{Ar}_{\text{K}}$ spectra of rhyolite samples 19ROM13 and 19ROM15 from Romanèche deposit.

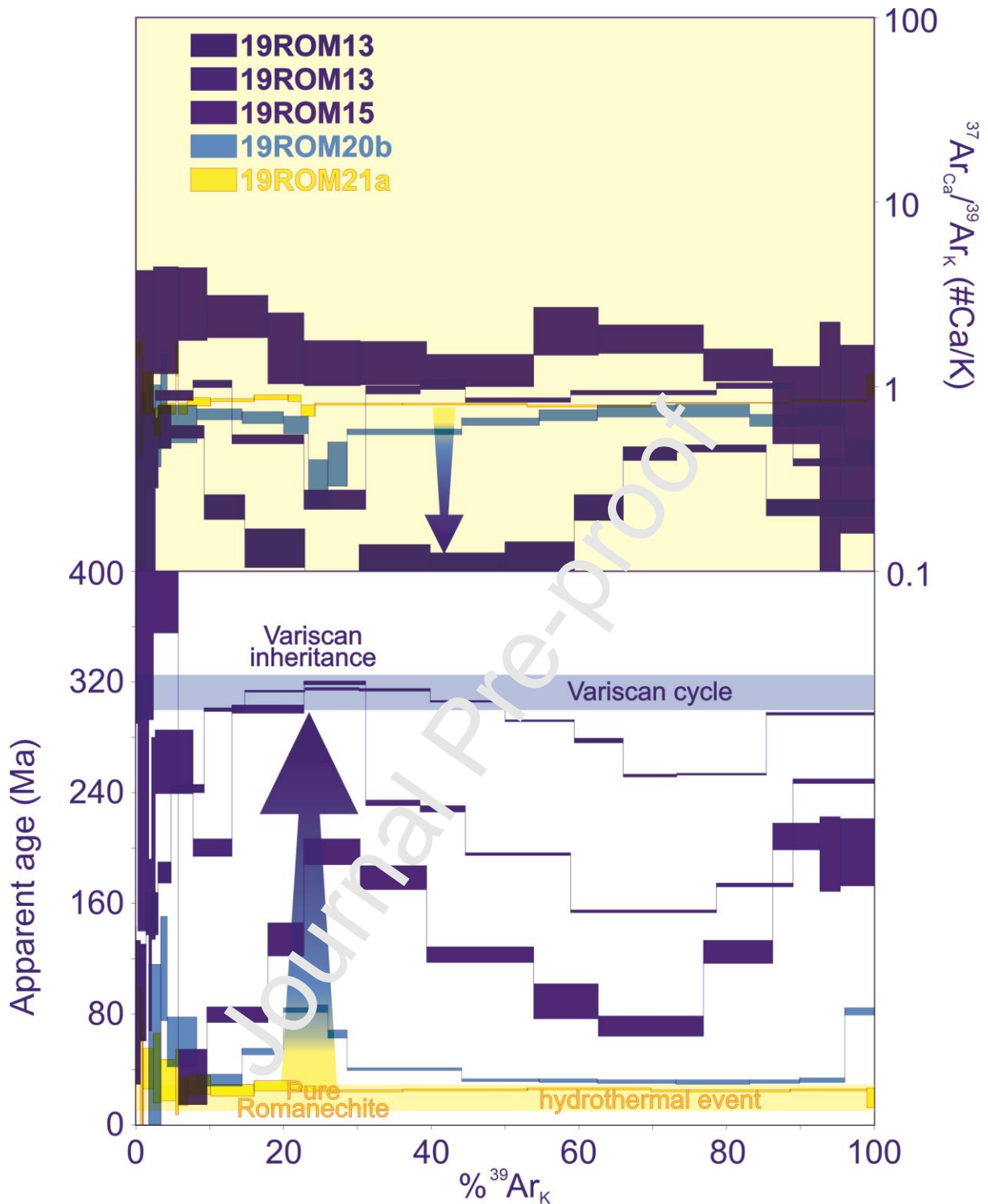


Fig. 8. Compilation of age spectra showing the inverse correlation in the low to intermediate temperature degassing domain between apparent ages and $^{37}\text{Ar}_{\text{Ca}}/^{39}\text{Ar}_{\text{K}}$ (# Ca/K) ratios.

The low-temperature steps (0-10% of $^{39}\text{Ar}_{\text{K}}$) of these age spectra are characterised by notably high rates and amounts of atmospheric argon, as shown by the clusters of points along the $^{36}\text{Ar}/^{40}\text{Ar}$ axis of the inverse isochron diagrams, as well as by anomalously high apparent ages that decrease rapidly (Fig. 6). These low temperature disturbances could express the

degassing of poorly crystallized phases or very small crystallites affected by $^{39}\text{Ar}_K$ recoil during the irradiation process (Ruffet et al., 1996; Vasconcelos, 1999).

Analyses of samples 19ROM13, 19ROM15 and duplicate 19ROM20b (19ROM20b-2) produce disturbed age spectra with low to high temperature steps that trace a hump followed by a saddle (Fig. 7). Maximum apparent ages from duplicate analyses of romanechite from sample 19ROM13, which cannot exceed the age of Jurassic carbonates, are consistent with the age of the host granite, at c. 320 Ma, and suggest contamination by Variscan material, probably K-feldspars, which was not detected during the Mn oxide selection process. The shape of their $^{37}\text{Ar}_{\text{Ca}}/^{39}\text{Ar}_K$ (# Ca/K) spectra is antithetical, with the lowest ratios (about 0.1) yielded by steps with the oldest apparent ages and conversely for the highest ratios (about 1) which are provided by the constitutive steps of the saddle basements (Fig. 7). These observations suggest that the first stage of the degassing of these samples is dominated by the contaminating phase, old and Ca-poor, such as K-feldspars, while the second stage is dominated by degassing of the romanechite, younger and Ca-rich. This interpretation most likely applies to all the disturbed age spectra identified in this study, which have similar shapes but with varying amplitudes depending on the relative proportions of contaminating and romanechite phases, as shown in Figure 8. The decrease of the apparent age and the progressive attenuation of their sigmoidal shape are correlated with the progressive increase and flattening of the corresponding $^{37}\text{Ar}_{\text{Ca}}/^{39}\text{Ar}_K$ spectra. This trend leads to perfectly flat age and $^{37}\text{Ar}_{\text{Ca}}/^{39}\text{Ar}_K$ spectra that show the degassing of pure romanechite (e.g., 19ROM21a; Fig. 8), free of any Variscan contamination. The slightly higher values of the $^{37}\text{Ar}_{\text{Ca}}/^{39}\text{Ar}_K$ ratios of romanechite 19ROM15 and 19ROM23 suggest that fluorite (CaF_2) may have interfered with the outgassing of $^{37}\text{Ar}_{\text{Ca}}$, artificially increasing the measured Ca/K ratios (Fig. 8).

The new results (Figs. 6 and 9) and those which were obtained by Hautmann and Lippolt (2000) at 25.8 ± 0.4 , 24.9 ± 0.4 , 20.9 ± 0.7 and 20.8 ± 0.6 Ma cover a period of 7.6 Ma, between 25.8 ± 0.4 Ma and 18.2 ± 0.5 Ma (Fig. 9). It is not possible, at this stage, to determine whether the mineralization process was continuous or discontinuous and whether its duration was fully recorded.

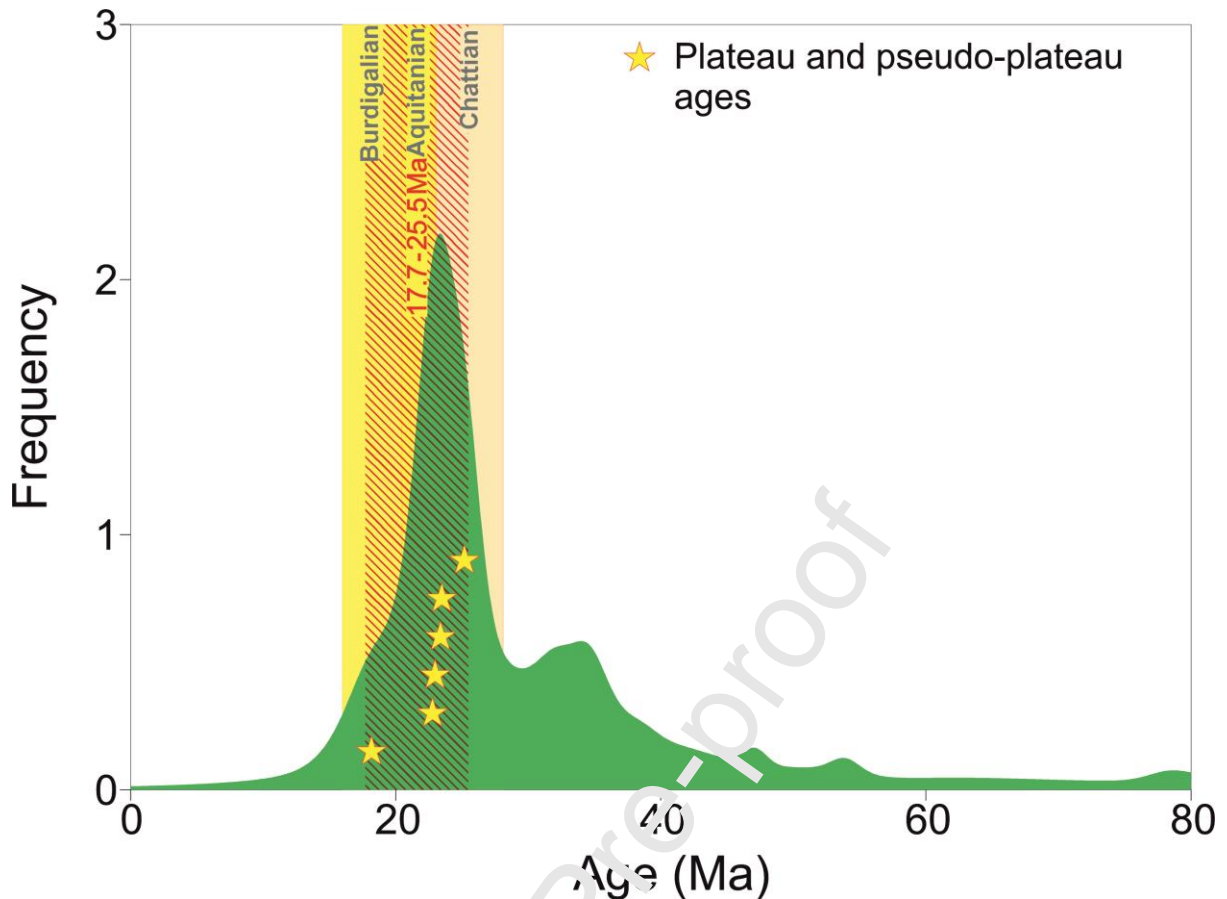


Fig. 9. Frequency (probability density) diagrams of apparent ages of resized age spectra (steps of 5% of $^{39}\text{Ar}_K$ released ; see Le Putter and Ruffet (2020) and Tremblay et al. (2020) for explanation). Validated ages (plateau and pseudo-plateau ages) are plotted as yellow stars (error bars are smaller than the size of the symbols).

6. Discussion

6.1 Ore deposit model

Romanechite has been described in various environments, from weathering crusts to hydrothermal deposits (Dill, 2010; Nicholson, 1992; Perseil and Pinet, 1976). First considered as a supergene gossan capping an underlying and hidden hydrothermal mineralization (Dolomieu, 1796; Drouot, 1857; Hautmann and Lippolt, 2000; Lacroix, 1910; Lougnon, 1981), the new geochemical and petrographical data from this study support a fault-controlled hydrothermal formation of the romanechite ore.

The fluorite-barite gangue is common in hydrothermal Mn deposits (Hewett, 1966, 1964; Holtstam and Mansfeld, 2001; Leal et al., 2008; Roy, 1981, 1968) whereas it is unusual in other genetic types such as sedimentary, metamorphic or supergene deposits (Dill, 2010; Kuleshov, 2016; Maynard, 2014; Varentsov, 1996). In addition, silicification is the form of

wall-rock alteration associated with the Mn oxide ore (Hewett, 1964). Quartz precipitates either before or after the Mn oxide within the ore zone (Figs. 3i, 3j and 4).

The Mn ore is trapped in and coplanar with the major fault zone (Figs. 1b and 2). Relation with tectonics is expressed in the ore by a breccia composed of granite fragments cemented by romanechite and gangue minerals (Fig. 3c). The Mn ore is itself brecciated and cemented by successive generations of romanechite (Figs. 3h and i). In addition, the clayey zone at the wall of the Mn vein contains fragments of the Jurassic limestones (Lougnon, 1981) and the romanechite ore (Fig. 2, Bouladon, 1958). Accordingly, this fault was active several times before and after the Mn ore deposition.

Dissolution of fluorite inside romanechite (Fig. 3n) and its (re)deposition as a coating on romanechite (Fig. 4, Chermette, 1975) supports that romanechite was formed in the same temperature range than fluorite. These temperatures are most likely between 100-200°C, according to data from other epithermal Mn deposits having similar mineralogical composition (Glasby et al., 2005; Hewett, 1964; Hewett et al., 1963; Hewett and Fleischer, 1960; Leal et al., 2008; Liakopoulos et al., 2001; Madondo et al., 2020; Papavassiliou et al., 2017; Voudouris et al., 2021). The dissolved fluorite crystals observed in some parts of the Romanèche deposit (Fig. 3n) suggests that acidic fluids post-dated romanechite precipitation (Richardson and Holland, 1979; Zhang et al., 2006). Low pH did not remobilize the Mn hosted in romanechite because the high Eh was maintained under prevailing sub-surface conditions.

Mineral zoning is clearly established in space and time with the occurrence of Fe oxides at depth and tetravalent Mn oxides in the upper levels of the mineralization (Fig. 2, Bouladon, 1958). This trend is also materialized by the successive crystallization of hematite, arseniosiderite, romanechite and coronadite group minerals (Fig. 4). The vertical mineral zoning appears to be controlled by the O₂ conditions and cooling of the ascending hydrothermal solution (Hewett, 1966; Perseil and Pinet, 1976). This O₂ and temperature dependency is responsible for the separation of Fe from Mn in the vertical sequence. Seemingly, the Romanèche ore corresponds to the uppermost part of the hydrothermal system as no reduced Mn^{2+/3+}-bearing minerals (sulphides, carbonates or silicates) have been reported.

As such, romanechite precipitated in an open system (Figs. 3a, b, c and f), directly from the mineralizing fluid and not by replacement of lower valence Mn-bearing minerals as observed

in other subsurface Mn oxide ores (Dekoninck et al., 2021, 2019, 2016; Lafforgue et al., 2021). In this context, it is unlikely that the romanechite-bearing ore derived from *in situ* supergene weathering such as in gossan.

Geochemical analyses of samples from the Romanèche deposit show an enrichment in Mn-Ba-As-W (Table 1; Fig. 5a), which is consistent with the Mn-As-Ba-Sr enrichment observed in epithermal Mn deposits (Glasby et al., 2005; Hewett et al., 1963). The ternary plot of Bonatti et al. (1972) and the Nicholson's discrimination diagram (Nicholson, 1992) support the hydrothermal origin of the Mn ore, and in particular the strong enrichment in As and other trace metals (Fig. 10, Tables 1 and 2). Nevertheless, these plots cannot be used as a proof of origin because Mn oxides from the supergene zone of polymetallic deposits may also carry a high metal content without being of hydrothermal origin (Vasconcelos, 2002). However, the Romanèche Mn deposit does not contain ore-forming minerals hosting high amounts of metals, such as sulphides as the primary source of metals. Instead, the Mn ore is predominantly composed of romanechite and hercynite at depth (Fig. 2). Therefore, the geochemistry of the romanechite ore would represent the composition of the fluid from which it has precipitated. In addition, the substantial enrichment in W, up to 1.4 wt.% (Table 1), is consistent with data from hydrothermal epithermal Mn oxide deposits having similar mineralogy and geochemistry (Glasby et al., 2005; Holtstam and Mansfeld, 2001). Tungsten enrichment is usually connected to volcanogenic-magmatic process (i.e. skarns, pegmatite, porphyries, VMS) and has a particular affinity with manganese to form the wolframite series (Dill, 2010). Tungsten-rich romanechite vein-type mineralization hosted in granite may indicate a direct contribution of magmatic fluids in the geochemistry of the ore. Either the low content of W of the mineralizing fluid, the low temperature and the high O₂ fugacity may prevent the precipitation of W-rich minerals, such as wolframite. However, the source of the Mn-Ba-As-W remains elusive, but O₂-poor acidic fluids would transport the metals regardless of their origin.

6.2 Interpretation of romanechite radiometric ages

Hautmann and Lippolt (2000) previously dated four romanechite samples at 25.8±0.4, 24.9±0.4, 20.9±0.7 and 20.8±0.6 Ma which they interpret as a record of a long weathering event (Table 3). However, this interpretation fails to explain some of the key observations described above (Fig. 10): romanechite formed by ascending circulation of hot mineralizing fluids. The new ⁴⁰Ar/³⁹Ar ages between 25.2±0.3 to 18.2±0.5 Ma (Fig. 6) combined with

those obtained by Hautmann and Lippolt (2000) highlight mineralizing events from late Chattian to early Burdigalian (Table 3). It is unlikely that the hydrothermal ore system was active continuously during c. 7.6 My. We rather hypothesize several pulses at ~25 Ma, ~23 Ma, ~21 Ma and ~18 Ma. Therefore, the romanechite ages attest to a regular hydrothermal activity over at least c. 7.6 My along the fault zone delimiting the contact between the MC and the Bresse graben. Therefore, it is also likely that our age data is a testimony of the (re)activation age of the fault system. This study further confirms the reliability of the $^{40}\text{Ar}/^{39}\text{Ar}$ dating of romanechite in hydrothermal Mn ore.

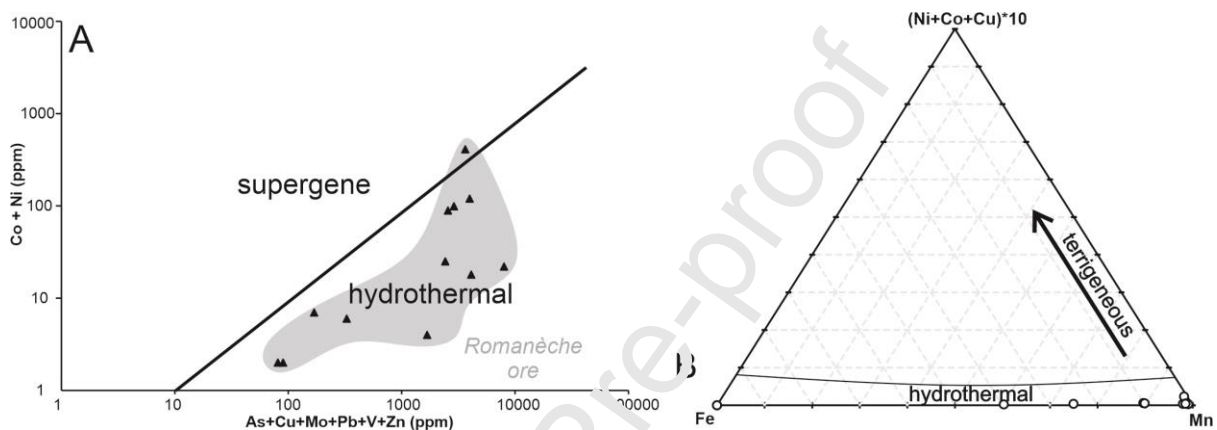


Fig. 10. a. Diagnostic plot of hydrothermal geochemical signature for Mn deposits (Nicholson, 1992) applied to the Romanèche Mn deposit. **b.** Mn-Fe-(Ni+Cu+Co) ternary differentiation diagram (mass basis) for marine hydrogenetic and hydrothermal Mn oxides (Bonatti et al., 1972).

The western part of the European plate was affected by extensive rifting episodes during the Tertiary (Bois, 1993; Prud'homme et al., 2006; Ziegler, 1992). E-W extensional stress fields led to the formation of numerous grabens (Eger, Rhine, Limagne, Roanne-Montbrison, Bresse) from the late Eocene to the end of the early Miocene in and around the MC (Merle et al., 1998; Michon and Merle, 2001). The development of this major graben system (West European Rift System; Figs. 1a and b) is accompanied by typical intraplate alkaline volcanism occurring either within the grabens or along their margins (Wilson and Downes, 1991). An important syn-rift magmatism event took place in the northern MC from late Oligocene to early Miocene (Bellon, 1971; Chantepie, 1990; Michon and Merle, 2001) at a time when sedimentation declined in the grabens (Sissingh, 2001, 1998) and where the crust was the thinnest (Merle et al., 1998; Michon and Merle, 2001). This is why most of the late Oligocene volcanic activity is located near the Limagne graben (Fig. 1a) when almost no

volcanic activity occurred elsewhere. The magmatic process involved partial melting in an E-W extensional regime that reactivated N-S Variscan fault zones (Michon and Merle, 2001). The period covered by volcanic activity and reactivation of faults is perfectly coherent with the ~26-18 Ma period recovered from romanechite dating (Table 3).

The high heat flow beneath the MC (Lucazeau et al., 1984), materialized by intraplate magmatic activity probably enhanced circulation of hot mineralizing fluids. We support a primary hydrothermal activity related to the widespread volcanic activity to account for the unusual enrichment in some granitophile elements, such as tungsten (Fig. 5). As indeed high heat flow and widespread volcanism would contribute to hydrothermal activity in the area, we cannot rule out a SedEX-like formation process. The calculated thickness of ~3,000 meters of Cenozoic sediments in the Bresse Graben (Sissingu, 1998) would account for the generation of basinal fluids by compaction and their upward migration along the margins of the graben. The Mn-Ba-As-W enrichment observed in the romanechite ore (Fig. 5) may have been leached by hydrothermal fluids from the granitic basement rocks. In any case, the bordering fault zone channelled the mineralizing fluid precipitating an epithermal ore type. When these fluids cool and reach more oxygenated wet horizons (i.e., watertable), they precipitated the H₂O-rich Mn oxides (Glaby et al., 2005; Hewett, 1964). The Romanèche area is considered to be subaerial during the deposition of the Mn mineralization (Sissingu, 1998) and likely looked like a hot spring apron system. The Sinemurian carbonates host the epigenetic stratabound mineralization by fluid-rock interaction (Fig. 2).

Overall, it means that other fault-controlled mineralization may also be related to the hydrothermal events reported in this study. This would be true at least for the northern MC domain and possibly in connection with reactivated faults occurring along the West-European graben segments, where Oligocene-Miocene volcanic activity has been reported (i.e., Vosges, Black Forest; Wilson and Downes, 2006).

7. Conclusions

This study provides geochemical, petrographical and geological evidences for hydrothermal origin of the Romanèche manganese deposit. Careful ⁴⁰Ar/³⁹Ar dating of pure romanechite grains provides reliable plateau-ages between 26 Ma and 18 Ma, corresponding to various pulses of hydrothermal activity. This study confirms the great applicability of this mineral for geochronological studies, despite its relatively low K content (0.1-0.6 wt.% K). The good crystallinity of romanechite due to its hydrothermal formation likely favours a better

production and/or retention of the radiogenic argon than poorly crystallized phases of supergene origin. The age of the hydrothermal system of Romanèche is coeval with graben-related fault reactivation and distant volcanic activity in the northern Massif Central, which provides time constrain for fault-related mineralization events along the Massif Central, and possibly along the West-European graben segments.

Acknowledgment

This work was funded and carried out in the framework of the BRGM-TOTAL project Source-to-Sink. We appreciate the help of Prof. J. Wouters and Dr. N. Tumanov of the PC2 platform (UNamur) for collecting XRD patterns. This research also used the resources of the Electron Microscopy Service located at the University of Namur (“Plateforme Technologique Morphologie — Imagerie”). We are delighted to Ir. Pieter V’Hoest of the Department of Materials Engineering at the Katholieke Universiteit Leuven (KUL) for some of the EPMA analyses. We are also delighted to two anonymous reviewers who have greatly improved this manuscript.

Appendix A. Supplementary Material

1. EPMA analytical conditions and standards used for quantification
2. Sample list and main mineralogy
3. Position of the spots collected under back scattered views of samples 19ROM15 and 19ROM32A.
4. BSE views of the grains selected for $^{40}\text{Ar}/^{39}\text{Ar}$ dating.
5. Hand specimen photographs
6. Field photographs
7. Research data

References

- Beauvais, A., Chardon, D., 2013. Modes, tempo, and spatial variability of Cenozoic cratonic denudation: The West African example. *Geochemistry, Geophysics, Geosystems* 14, 1590–1608. <https://doi.org/10.1002/ggge.20093>
- Bellon, H., 1971. Datation absolue de laves d'Auvergne par la méthode potassium–argon (Ph.D thesis). Université Paris Sud, Orsay.
- Bois, C., 1993. Initiation and evolution of the Oligo-Miocene rift basins of southwestern Europe: Contribution of deep seismic reflection profiling. *Tectonophysics, The origin of sedimentary basins: Inferences from quantitative modelling and basin analysis* 226, 227–252. [https://doi.org/10.1016/0040-1951\(93\)90120-2](https://doi.org/10.1016/0040-1951(93)90120-2)
- Bonatti, E., Kraemer, T., Rydell, H., 1972. Classification and Genesis of Submarine Iron-Manganese Deposits., in: Horn, D.R. (Ed.), *Ferric manganese Deposits on the Ocean Floor*. National Science Foundation, Washington, DC, pp. 149–166.
- Bouladon, J., 1958. Etude sommaire du gisement de manganèse de Romanèche (Saône-et-Loire) (No. A1390-2). Bureau de recherches géologiques, géophysiques et minières, Paris.
- Burns, R.G., Burns, V.M., 1979. Manganese oxides, in: *Marine Minerals*. Mineral Society of America, Washington DC, pp. 1–16.
- Chantepie, M., 1990. Le volcanisme tertiaire miocène et pliocène dispersé dans la région de Clermont et sur le plateau des Dômes : étude pétrologique et géochronologique (Mémoire DEA). Université de Clermont-Ferrand, Clermont-Ferrand.
- Chantraine, J., Autran, A., Cavalier, C., 2003. Carte géologique de la France à 1/1 000 000.
- Cheilletz, A., Ruffet, G., Maignac, C., Kolli, O., Gasquet, D., Féraud, G., Bouillin, J.P., 1999. $^{40}\text{Ar}/^{39}\text{Ar}$ dating of shear zones in the Variscan basement of Greater Kabylia (Algeria). Evidence of an Eo-Alpine event at 128 Ma (Hauterivian-Barremian boundary): Geodynamic consequences. *Tectonophysics* 306, 97–116. [https://doi.org/10.1016/S0040-1951\(99\)00047-5](https://doi.org/10.1016/S0040-1951(99)00047-5)
- Chermette, A., 1975. L'ancienne mine de manganèse de Romanèche (Saône-et-Loire). *Publications de la Société Linnéenne de Lyon* 44, 1–11. <https://doi.org/10.3406/linly.1975.10171>
- Choubert, G., Faure-Muret, A., 1973. The Precambrian iron and manganese deposits of the Anti-Atlas, in: *Genesis of Precambrian Iron and Manganese Deposits*. Presented at the Unesco Earth Sciences Symposium, Kiev, pp. 115–124.

- Conly, A.G., Scott, S.D., Bellon, H., 2011. Metalliferous Manganese Oxide Mineralization Associated with the Boléo Cu-Co-Zn District, Mexico. *Economic Geology* 106, 1173–1196. <https://doi.org/10.2113/econgeo.106.7.1173>
- De Putter, T., Ruffet, G., 2020. Supergene manganese ore records 75 Myr-long Campanian to Pleistocene geodynamic evolution and weathering history of the Central African Great Lakes Region – Tectonics drives, climate assists. *Gondwana Research* 83, 96–117. <https://doi.org/10.1016/j.gr.2020.01.021>
- Deckart, K., Féraud, G., Bertrand, H., 1997. Age of Jurassic continental tholeiites of French Guyana, Surinam and Guinea: Implications for the initial opening of the Central Atlantic Ocean. *Earth and Planetary Science Letters* 150, 205–220. [https://doi.org/10.1016/S0012-821X\(97\)00102-7](https://doi.org/10.1016/S0012-821X(97)00102-7)
- Decrée, S., Ruffet, G., Putter, T.D., Baele, J.-M., Recourt, P., Jamoussi, F., Yans, J., 2010. Mn oxides as efficient traps for metal pollutants in a polyphase low-temperature Pliocene environment: A case study in the Tamra iron mine, Nefza mining district, Tunisia. *Journal of African Earth Sciences* 57, 249–261. <https://doi.org/10.1016/j.jafrearsci.2009.08.005>
- Dekoninck, A., Bernard, A., Barbarand, J., Saint-Bezar, B., Missenard, Y., Lepretre, R., Saddiqi, O., Yans, J., 2016. Detailed mineralogy and petrology of manganese oxyhydroxide deposits of the Irani district (Morocco). *Mineralium Deposita* 51, 13–23. <https://doi.org/10.1007/s00126-015-0590-3>
- Dekoninck, A., Monié, P., Bloemans, S., Hatert, F., Rochez, G., Yans, J., 2019. Genesis and $^{40}\text{Ar}/^{39}\text{Ar}$ dating of K-Mn oxides from the Stavelot Massif (Ardenne, Belgium): Insights into Oligocene to Pliocene weathering periods in Western Europe. *Ore Geology Reviews* 115, 103–191. <https://doi.org/10.1016/j.oregeorev.2019.103191>
- Dekoninck, A., Moussi, B., Vennemann, T., Jamoussi, F., Mattielli, N., Decrée, S., Chافتar, H.-R., Hatira, N., Yans, J., 2018. Mixed hydrothermal and meteoric fluids evidenced by unusual H- and O-isotope compositions of kaolinite-halloysite in the Fe(-Mn) Tamra deposit (Nefza district, NW Tunisia). *Applied Clay Science* 163, 33–45. <https://doi.org/10.1016/j.clay.2018.07.007>
- Dekoninck, A., Ruffet, G., Missenard, Y., Parizot, O., Magoua, M., Mouttaqi, A., Rochez, Gaëtan, Yans, J., 2021. Multistage genesis of the late Cretaceous manganese karst-hosted Tasdremt deposit (High Atlas, Morocco). *Mineralium Deposita* 59, 935–956. <https://doi.org/10.1007/s00126-020-01017-0>

- Deng, X.-D., Li, J.-W., Vasconcelos, P.M., 2016. $^{40}\text{Ar}/^{39}\text{Ar}$ dating of supergene Mn-oxides from the Zunyi Mn deposit, Guizhou Plateau, SW China: Implications for chemical weathering and paleoclimatic evolution since the late Miocene. *Chemical Geology* 445, 185–198. <https://doi.org/10.1016/j.chemgeo.2016.02.009>
- Dill, H.G., 2010. The “chessboard” classification scheme of mineral deposits: Mineralogy and geology from aluminum to zirconium. *Earth-Science Reviews* 100, 1–420. <https://doi.org/10.1016/j.earscirev.2009.10.011>
- Dolomieu, D., 1796. Description de la mine de manganèse de Romanèche. *Journal des Mines* 2, 14–26.
- Drouot, M., 1857. Les gîtes de houille et les terrains des environs des forges et de la Chapelle-sous-Dun et sur les gîtes de manganèse et les terrains des environs de Romanèche. Conseil général des mines, Imprimerie Impériale 109–214.
- Dufrénoy, A., 1842. Description de l’arsénio-sidérite, nouvelle espèce d’arséniat de fer. *Annales des mines* 2, 343–346.
- Fusswinkel, T., Wagner, T., Wenzel, T., Wälle, M., Lorenz, J., 2013. Evolution of unconformity-related MnFeAs vein mineralization, Sailauf (Germany): Insight from major and trace elements in oxide and carbonate minerals. *Ore Geology Reviews* 50, 28–51. <https://doi.org/10.1016/j.oregeorev.2012.08.001>
- Glasby, G.P., Papavassiliou, C.T., Mutton, J., Valsami-Jones, E., Liakopoulos, A., Renner, R.M., 2005. The Vani manganese deposit, Milos island, Greece: A fossil stratabound Mn–Ba–Pb–Zn–As–Sb–W-rich hydrothermal deposit, in: *Developments in Volcanology*. Elsevier, pp. 255–291. [https://doi.org/10.1016/S1871-644X\(05\)80045-2](https://doi.org/10.1016/S1871-644X(05)80045-2)
- Hanes, J.A., York, D., Hall, C.M., 1985. An $^{40}\text{Ar}/^{39}\text{Ar}$ geochronological and electron microprobe investigation of an Archaean pyroxenite and its bearing on ancient atmospheric compositions. *Canadian Journal of Earth Sciences* 22, 947–958. <https://doi.org/10.1139/e85-100>
- Hautmann, S., Lippolt, H.J., 2000. $^{40}\text{Ar}/^{39}\text{Ar}$ dating of central European K–Mn oxides — a chronological framework of supergene alteration processes during the Neogene. *Chemical Geology* 170, 37–80. [https://doi.org/10.1016/S0009-2541\(99\)00241-7](https://doi.org/10.1016/S0009-2541(99)00241-7)
- Hewett, D.F., 1966. Stratified deposits of the oxides and carbonates of manganese. *Economic Geology* 61, 431–461. <https://doi.org/10.2113/gsecongeo.61.3.431>
- Hewett, D.F., 1964. Veins of hypogene manganese oxide minerals in the southwestern United States. *Economic Geology* 59, 1429–1472. <https://doi.org/10.2113/gsecongeo.59.8.1429>

- Hewett, D.F., Fleischer, M., 1960. Deposits of the manganese oxides. *Economic Geology* 55, 1–55. <https://doi.org/10.2113/gsecongeo.55.1.1>
- Hewett, D.F., Fleischer, M., Conklin, N., 1963. Deposits of the manganese oxides; supplement. *Economic Geology* 58, 1–51. <https://doi.org/10.2113/gsecongeo.58.1.1>
- Holtstam, D., Mansfeld, J., 2001. Origin of a carbonate-hosted Fe-Mn-(Ba-As-Pb-Sb-W) deposit of Långban-type in central Sweden. *Min Dep* 36, 641–657. <https://doi.org/10.1007/s001260100183>
- Jean, A., Beauvais, A., Chardon, D., Arnaud, N., Jayananda, M., Mathe, P.E., 2019. Weathering history and landscape evolution of Western Ghats (India) from $^{40}\text{Ar}/^{39}\text{Ar}$ dating of supergene K–Mn oxides. *Journal of the Geological Society*. <https://doi.org/10.1144/jgs2019-048>
- Kuleshov, V., 2016. Isotope geochemistry: the origin and formation of manganese rocks and ores. Elsevier, Amsterdam Boston Heidelberg London New York Oxford Paris San Diego San Francisco Singapore Sydney Tokyo.
- Lacroix, A., 1910. *Minéralogie de la France et de ses colonies: description physique et chimique des minéraux, étude des conditions géologiques et leurs gisements*, Librairie Polytechnique, Ch. Béranger. ed, Tome 4. Librairie Polytechnique, Paris.
- Lafforgue, L., Dekoninck, A., Barbarand, J., Brigaud, B., Bouabdellah, M., Verhaert, M., Mouttaqi, A., Yans, J., 2021. Geological and geochemical constrains on the genesis of the sedimentary-hosted Bou Arra Mn(-Fe) deposit (Eastern High Atlas, Morocco). *Ore Geology Reviews* 133, 104094. <https://doi.org/10.1016/j.oregeorev.2021.104094>
- Leal, P.R., Correa, M.J., Anetruo, S.J., Etcheverry, R.O., de Brodtkorb, M.K., 2008. The manganese deposits of the Pampean Ranges, Argentina. *The Canadian Mineralogist* 46, 1215–1233. <https://doi.org/10.3749/canmin.46.5.1215>
- Lee, J.-Y., Marti, K., Severinghaus, J.P., Kawamura, K., Yoo, H.-S., Lee, J.B., Kim, J.S., 2006. A redetermination of the isotopic abundances of atmospheric Ar. *Geochimica et Cosmochimica Acta* 70, 4507–4512. <https://doi.org/10.1016/j.gca.2006.06.1563>
- Li, J.-W., Vasconcelos, P., Duzgoren-Aydin, N., Yan, D.-R., Zhang, W., Deng, X.-D., Zhao, X.-F., Zeng, Z.-P., Hu, M.-A., 2007. Neogene weathering and supergene manganese enrichment in subtropical South China: An $^{40}\text{Ar}/^{39}\text{Ar}$ approach and paleoclimatic significance. *Earth and Planetary Science Letters* 256, 389–402. <https://doi.org/10.1016/j.epsl.2007.01.021>

- Liakopoulos, A., Glasby, G.P., Papavassiliou, C.T., Boulegue, J., 2001. Nature and origin of the Vani manganese deposit, Milos, Greece: an overview. *Ore Geology Reviews* 18, 181–209. [https://doi.org/10.1016/S0169-1368\(01\)00029-4](https://doi.org/10.1016/S0169-1368(01)00029-4)
- Lippolt, H.J., Hautmann, S., 1995. $^{40}\text{Ar}/^{39}\text{Ar}$ ages of Precambrian manganese ore minerals from Sweden, India and Morocco. *Mineralium Deposita* 30, 246–256. <https://doi.org/10.1007/BF00196360>
- Lougnon, J., 1981. Ressources minières françaises : les gisements de manganèse (Bureau de Recherches Géologiques et Minières No. Tome 10). BRGM.
- Lucazeau, F., Vasseur, G., Bayer, R., 1984. Interpretation of heat flow data in the french massif central. *Tectonophysics, Terrestrial Heat Flow Studies and the Structure of the Lithosphere* 103, 99–119. [https://doi.org/10.1016/0040-1951\(84\)90077-5](https://doi.org/10.1016/0040-1951(84)90077-5)
- Madondo, J., Canet, C., González-Partida, E., Rodríguez-Íñaz, A.A., Núñez-Useche, F., Alfonso, P., Rajabi, A., Pi, T., Blignaut, L., Vafeas, N., 2020. Geochemical constraints on the genesis of the ‘Montaña de Manganeso’ vein-type Mn deposit, Mexican Plateau. *Ore Geology Reviews* 123, 103680. <https://doi.org/10.1016/j.oregeorev.2020.103680>
- Maynard, J.B., 2014. Manganiferous sediments, rocks, and ores, in: *Treatise on Geochemistry*. Elsevier, pp. 327–349.
- McLennan, S.M., 2001. Relationships between the trace element composition of sedimentary rocks and upper continental crust. *Geochemistry, Geophysics, Geosystems* 2, 24. <https://doi.org/10.1029/2000GC000109>
- Merle, O., Michon, L., Carnus, G., Goer, A. de, 1998. L’extension oligocene sur la transversale septentrionale du rift du Massif central. *Bulletin de la Société Géologique de France* 169, 617–626.
- Michon, L., Merle, O., 2001. The evolution of the Massif Central Rift; spatio-temporal distribution of the volcanism. *Bulletin de la Société Géologique de France* 172, 201–211. <https://doi.org/10.2113/172.2.201>
- Nicholson, K., 1992. Contrasting mineralogical-geochemical signatures of manganese oxides; guides to metallogenesis. *Economic Geology* 87, 1253–1264. <https://doi.org/10.2113/gsecongeo.87.5.1253>
- O’Reilly, G.A., 1992. Petrographic and geochemical evidence for a hypogene origin of granite-hosted, vein-type Mn mineralization at the New Ross Mn deposits, Lunenburg County, Nova Scotia, Canada. *Economic Geology* 87, 1275–1300. <https://doi.org/10.2113/gsecongeo.87.5.1275>

- Papavassiliou, K., Voudouris, P., Kanellopoulos, C., Glasby, G., Alfieris, D., Mitsis, I., 2017. New geochemical and mineralogical constraints on the genesis of the Vani hydrothermal manganese deposit at NW Milos island, Greece: Comparison with the Aspro Gialoudi deposit and implications for the formation of the Milos manganese mineralization. *Ore Geology Reviews* 80, 594–611. <https://doi.org/10.1016/j.oregeorev.2016.07.023>
- Perseil, E.A., Pinet, M., 1976. Contribution à la connaissance des romanéchites et des cryptomélanes — coronadites — hollandites. Traits essentiels et paragenèses. *Contr. Mineral. and Petrol.* 55, 191–204. <https://doi.org/10.1007/BF00372226>
- Post, J.E., 1999. Manganese oxide minerals: crystal structures and economic and environmental significance. *Proceedings of the National Academy of Sciences* 96, 3447–3454. <https://doi.org/10.1073/pnas.96.7.3447>
- Prodehl, C., Mueller, St., Haak, V., 2006. The European Cenozoic rift system, in: *Continental Rifts: Evolution, Structure, Tectonics, Developments in Geotectonics*. Elsevier, pp. 133–212.
- Richardson, C.K., Holland, H.D., 1979. The solubility of fluorite in hydrothermal solutions, an experimental study. *Geochimica et Cosmochimica Acta* 43, 1313–1325. [https://doi.org/10.1016/0016-7037\(79\)90121-2](https://doi.org/10.1016/0016-7037(79)90121-2)
- Roddick, J.C., Cliff, R.A., Rex, D.C., 1980. The evolution of excess argon in alpine biotites - a ^{40}Ar - ^{39}Ar analysis. *Earth and Planetary Science Letters* 48, 185–208. [https://doi.org/10.1016/0012-821X\(80\)90181-8](https://doi.org/10.1016/0012-821X(80)90181-8)
- Roy, S., 1981. *Manganese Deposits*. Academic Press, London ; New York.
- Roy, S., 1968. Mineralogy of the different genetic types of manganese deposits. *Economic Geology* 63, 760–786. <https://doi.org/10.2113/gsecongeo.63.7.760>
- Ruffet, G., Féraud, G., Amouric, M., 1991. Comparison of ^{40}Ar - ^{39}Ar conventional and laser dating of biotites from the North Trégor Batholith. *Geochimica et Cosmochimica Acta* 55, 1675–1688. [https://doi.org/10.1016/0016-7037\(91\)90138-U](https://doi.org/10.1016/0016-7037(91)90138-U)
- Ruffet, G., Féraud, G., Balèvre, M., Kiénast, J.-R., 1995. Plateau ages and excess argon in phengites: an ^{40}Ar - ^{39}Ar laser probe study of Alpine micas (Sesia Zone, Western Alps, northern Italy). *Chemical Geology* 121, 327–343. [https://doi.org/10.1016/0009-2541\(94\)00132-R](https://doi.org/10.1016/0009-2541(94)00132-R)
- Ruffet, G., Gruau, G., Ballèvre, M., Féraud, G., Philippot, P., 1997. Rb/Sr and $^{40}\text{Ar}/^{39}\text{Ar}$ laser probe dating of high-pressure phengites from the Sesia zone (Western Alps): underscoring of excess argon and new age constraints on the high-pressure

- metamorphism. *Chemical Geology* 141, 1–18. [https://doi.org/10.1016/S0009-2541\(97\)00052-1](https://doi.org/10.1016/S0009-2541(97)00052-1)
- Ruffet, G., Innocent, C., Michard, A., Féraud, G., Beauvais, A., Nahon, D., Hamelin, B., 1996. A geochronological and study of K-Mn oxides from the weathering sequence of Azul, Brazil. *Geochimica et Cosmochimica Acta* 60, 2219–2232. [https://doi.org/10.1016/0016-7037\(96\)00080-4](https://doi.org/10.1016/0016-7037(96)00080-4)
- Sissingh, W., 2001. Tectonostratigraphy of the West Alpine Foreland: correlation of Tertiary sedimentary sequences, changes in eustatic sea-level and stress regimes. *Tectonophysics* 333, 361–400. [https://doi.org/10.1016/S0040-1951\(01\)00020-8](https://doi.org/10.1016/S0040-1951(01)00020-8)
- Sissingh, W., 1998. Comparative Tertiary stratigraphy of the Rhine Graben, Bresse Graben and Molasse Basin: correlation of Alpine foreland events. *Tectonophysics* 300, 249–284. [https://doi.org/10.1016/S0040-1951\(98\)00243-1](https://doi.org/10.1016/S0040-1951(98)00243-1)
- Tremblay, A., Ruffet, G., Lemarchand, J., 2020. Timing and duration of Archean orogenic gold deposits in the Bourlamaque pluton, Val d'Or mining camp, Abitibi, Canada. *Ore Geology Reviews* 127, 103812. <http://doi.org/10.1016/j.oregeorev.2020.103812>
- Turner, G., 1971. Argon 40-argon 39 dating: the optimization of irradiation parameters. *Earth and Planetary Science Letters* 10, 227–234. [https://doi.org/10.1016/0012-821X\(71\)90010-0](https://doi.org/10.1016/0012-821X(71)90010-0)
- Turner, S., Post, J.E., 1988. Refinement of the substructure and superstructure of romanechite. *American Mineralogist* 73, 1155–1161.
- Varentsov, I.M., 1996. Manganese ores of supergene zone: Geochemistry of formation, *Solid Earth Sciences Library*. Springer Netherlands, Dordrecht.
- Vasconcelos, P.M., 2002. Geochronology of Weathering in the Mt Isa and Charters Towers Regions, Northern Queensland (Open File Reports (OFRs) No. 139), CRC for Landscape Evolution & Mineral Exploration (LEME). University of Queensland, St Lucia.
- Vasconcelos, P.M., 1999. K-Ar and $^{40}\text{Ar}/^{39}\text{Ar}$ geochronology of weathering processes. *Annual Review of Earth and Planetary Sciences* 27, 183–229. <https://doi.org/10.1146/annurev.earth.27.1.183>
- Vasconcelos, P.M., Becker, T.A., Renne, P.R., Brimhall, G.H., 1992. Age and duration of weathering by $^{40}\text{K}/^{40}\text{Ar}$ and $^{40}\text{Ar}/^{39}\text{Ar}$ analysis of potassium-manganese oxides. *Science* 258, 451–455. <https://doi.org/10.1126/science.258.5081.451>

- Vasconcelos, P.M., Carmo, I. de O., 2018. Calibrating denudation chronology through $^{40}\text{Ar}/^{39}\text{Ar}$ weathering geochronology. *Earth-Science Reviews* 179, 411–435. <https://doi.org/10.1016/j.earscirev.2018.01.003>
- Vasconcelos, P.M., Heim, J.A., Farley, K.A., Monteiro, H., Waltenberg, K., 2013. $^{40}\text{Ar}/^{39}\text{Ar}$ and (U–Th)/He – $^4\text{He}/^3\text{He}$ geochronology of landscape evolution and channel iron deposit genesis at Lynn Peak, Western Australia. *Geochimica et Cosmochimica Acta* 117, 283–312. <https://doi.org/10.1016/j.gca.2013.03.037>
- Vasconcelos, P.M., Renne, P.R., Becker, T.A., Wenk, H.-R., 1995. Mechanisms and kinetics of atmospheric, radiogenic, and nucleogenic argon release from cryptomelane during analysis. *Geochimica et Cosmochimica Acta* 59, 2057–2070. [https://doi.org/10.1016/0016-7037\(95\)00126-3](https://doi.org/10.1016/0016-7037(95)00126-3)
- Vasconcelos, P.M., Renne, P.R., Brimhall, G.H., Becker, T.A., 1994. Direct dating of weathering phenomena by $^{40}\text{Ar}/^{39}\text{Ar}$ and K–Ar analysis of supergene K–Mn oxides. *Geochimica et Cosmochimica Acta* 58, 1635–1665. [https://doi.org/10.1016/0016-7037\(94\)90565-7](https://doi.org/10.1016/0016-7037(94)90565-7)
- Voudouris, P., Kati, M., Magganas, A., Keith, M., Valsami-Jones, E., Haase, K., Klemd, R., Nestmeyer, M., 2021. Arsenian Erythrite and Cinnabar from Active Submarine Nearshore Vents, Paleochori Bay, Milos Island, Greece. *Minerals* 11, 14. <https://doi.org/10.3390/min11010014>
- Wilson, M., Downes, H., 2006. Tertiary–Quaternary intra-plate magmatism in Europe and its relationship to mantle dynamics. *Geological Society, London, Memoirs* 32, 147–166. <https://doi.org/10.1144/GSL.MEM.2006.032.01.09>
- Wilson, M., Downes, H., 1991. Tertiary–Quaternary Extension-Related Alkaline Magmatism in Western and Central Europe. *Journal of Petrology* 32, 811–849. <https://doi.org/10.1093/petrology/32.4.811>
- Zhang, R., Hu, S., Zhang, X., 2006. Experimental Study of Dissolution Rates of Fluorite in HCl–H₂O Solutions. *Aquat Geochem* 12, 123–159. <https://doi.org/10.1007/s10498-005-3658-3>
- Ziegler, P.A., 1992. European Cenozoic rift system. *Tectonophysics* 208, 91–111. [https://doi.org/10.1016/0040-1951\(92\)90338-7](https://doi.org/10.1016/0040-1951(92)90338-7)

Author statement file

We confirm that this manuscript has not been published elsewhere and is not under consideration by another journal. All authors have approved the manuscript and agree with its submission to *Chemical Geology*. AD and GR actively co-written the article main body. JB and RW collected the samples from the field investigation, actively took part of the discussion and carefully revised former versions of the manuscript. S. Philippo helped access to analytical facilities (SEM-EDS), provided key samples of romanechite from the National Museum of Natural History collection and carefully revised former versions of the manuscript. O. Namur and Y. Zhang acquired the EPMA and revised the manuscript.

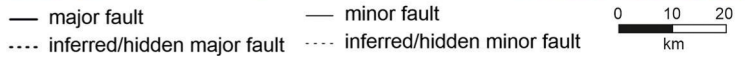
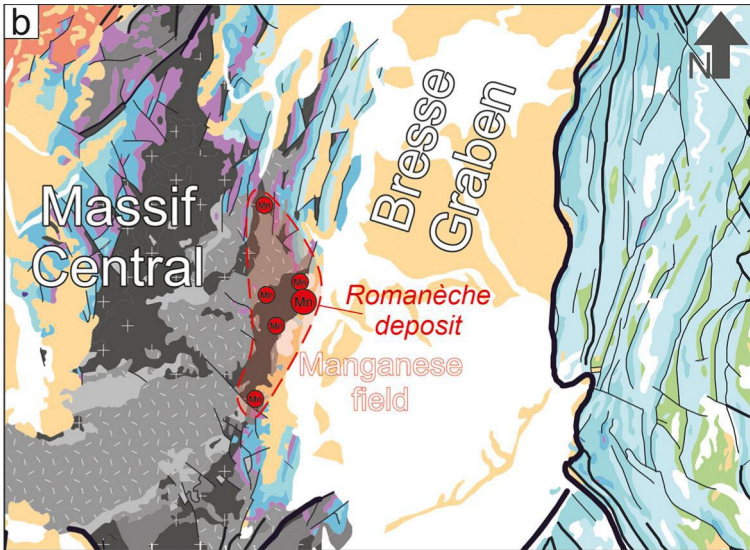
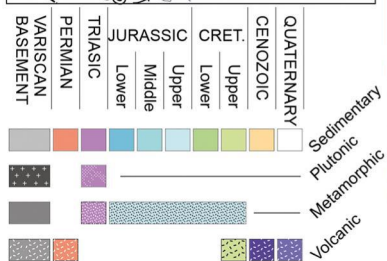
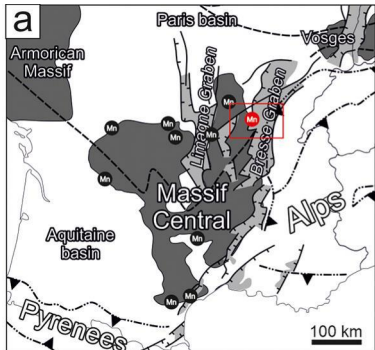


Figure 1

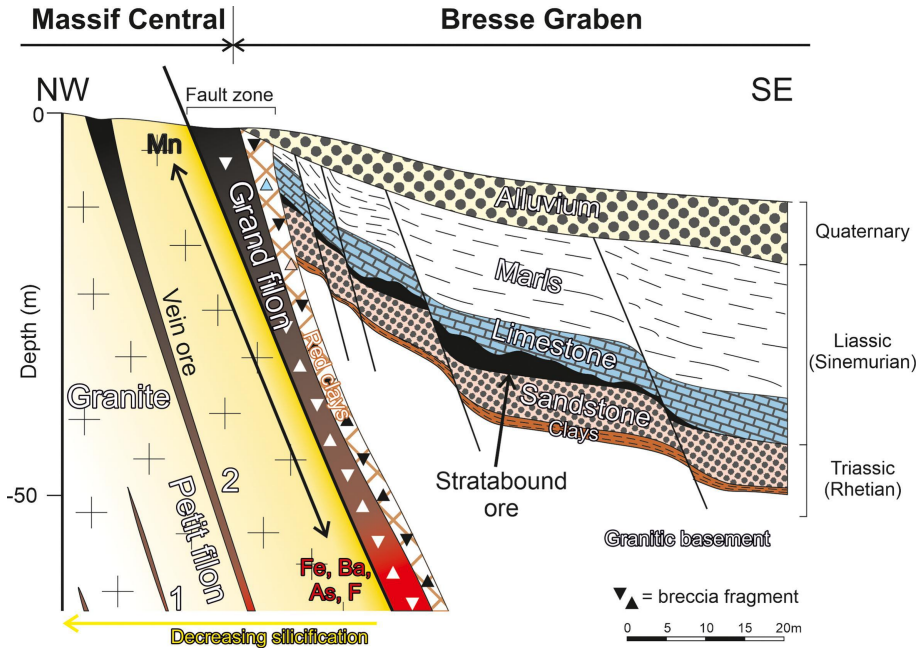


Figure 2

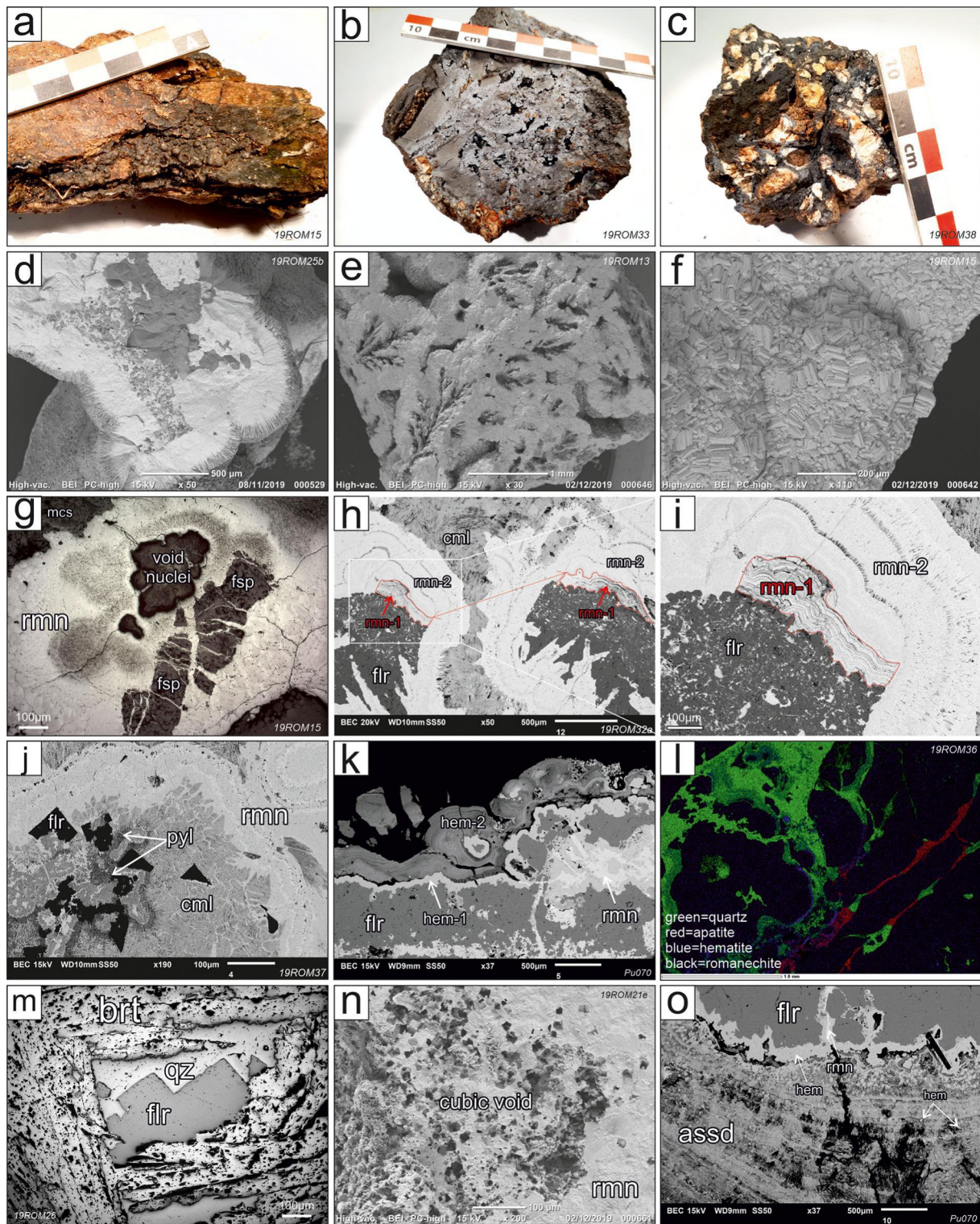


Figure 3

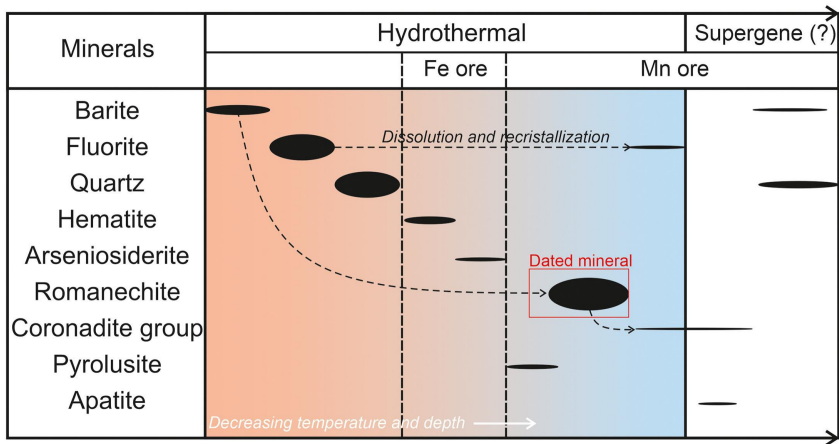


Figure 4

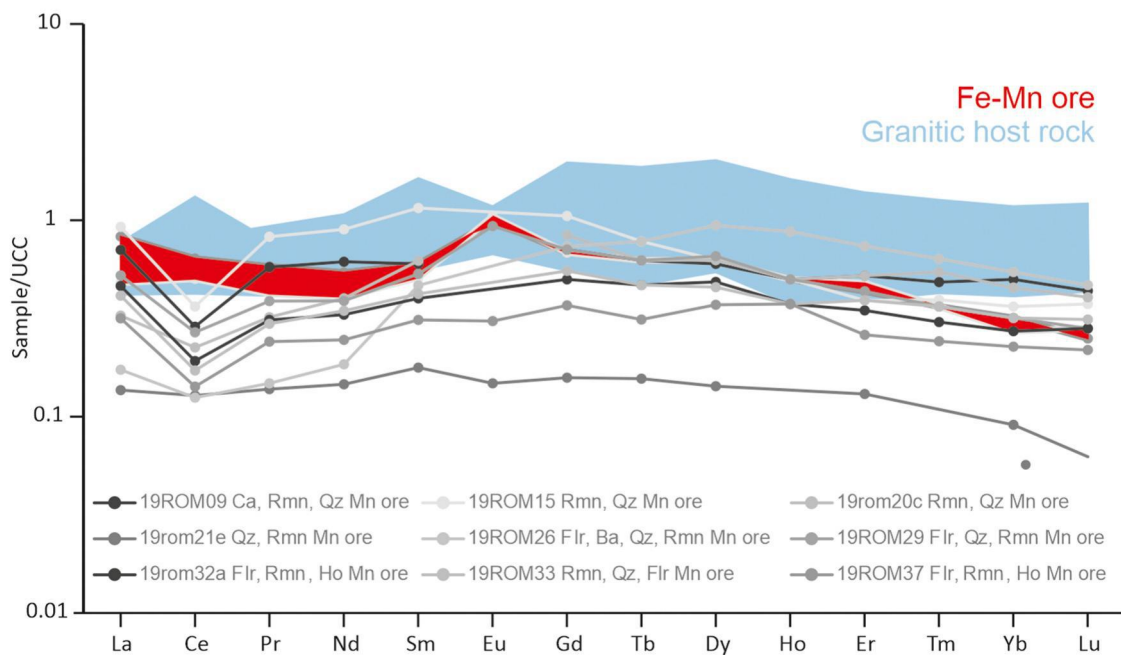
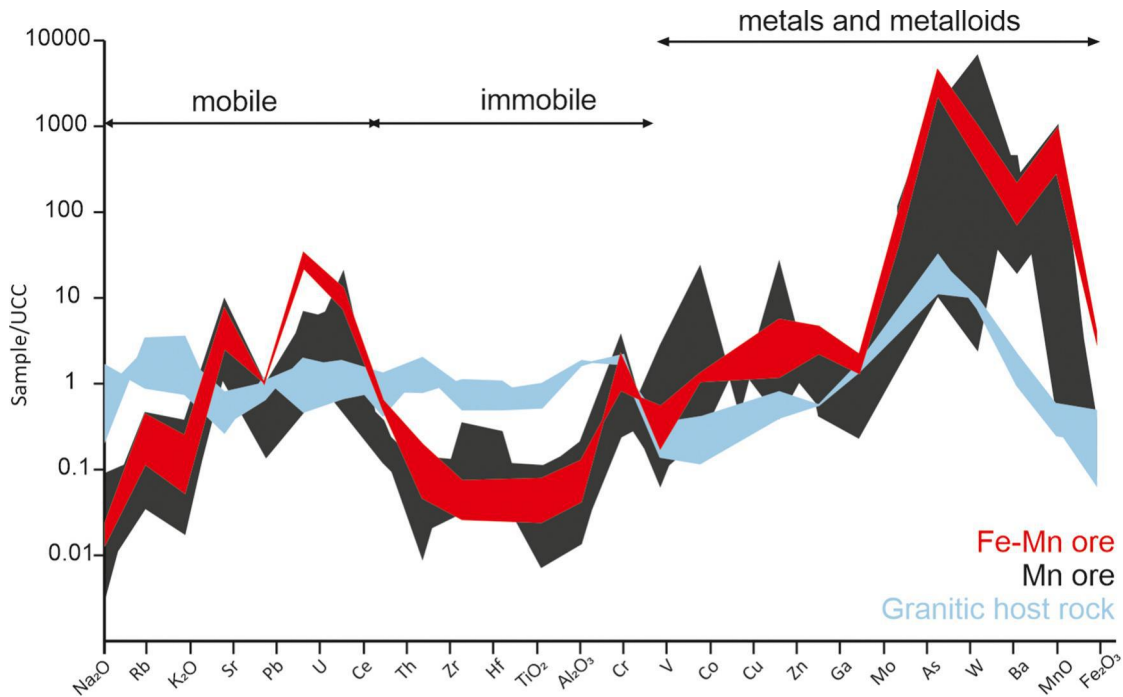


Figure 5

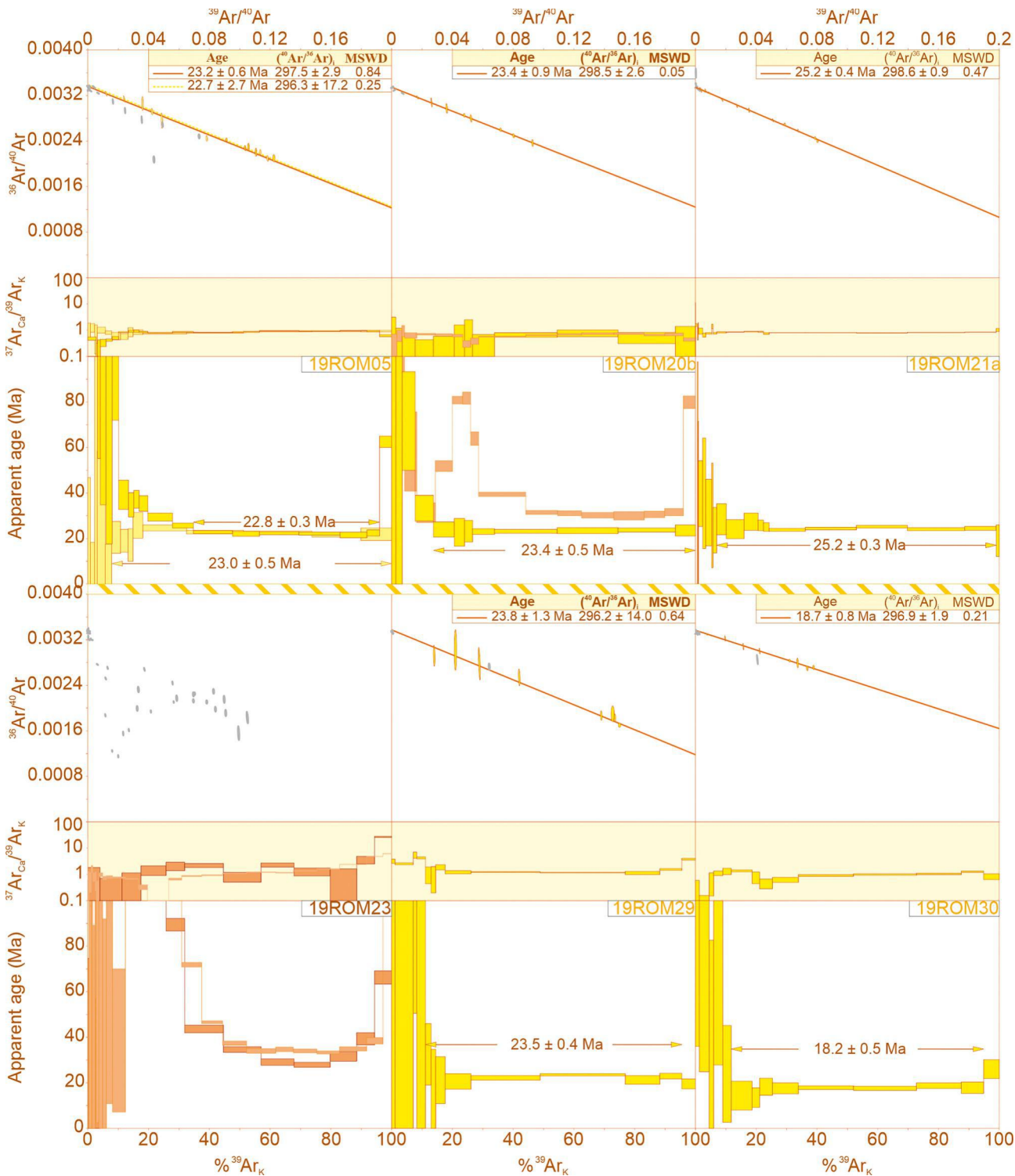


Figure 6

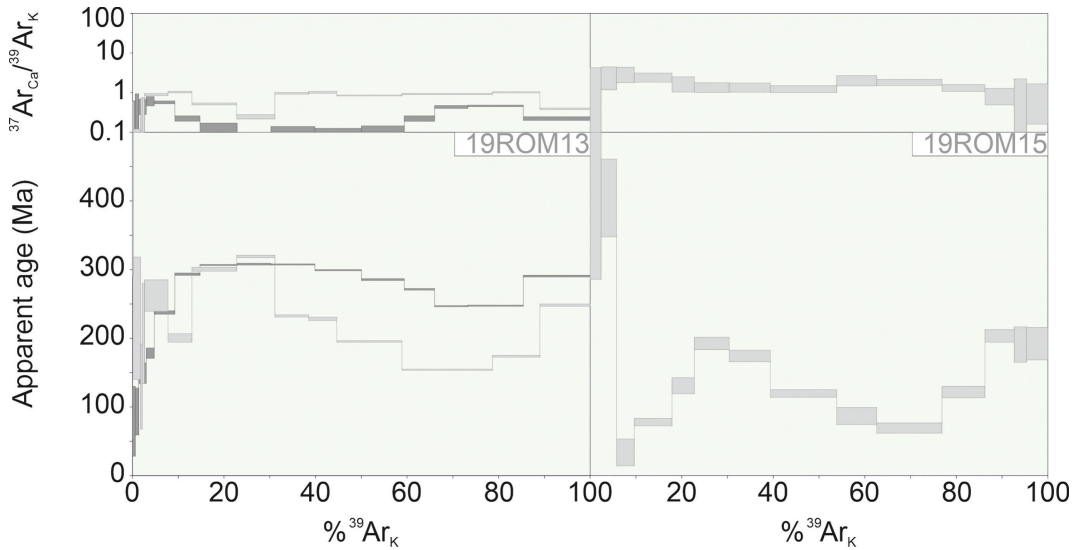


Figure 7

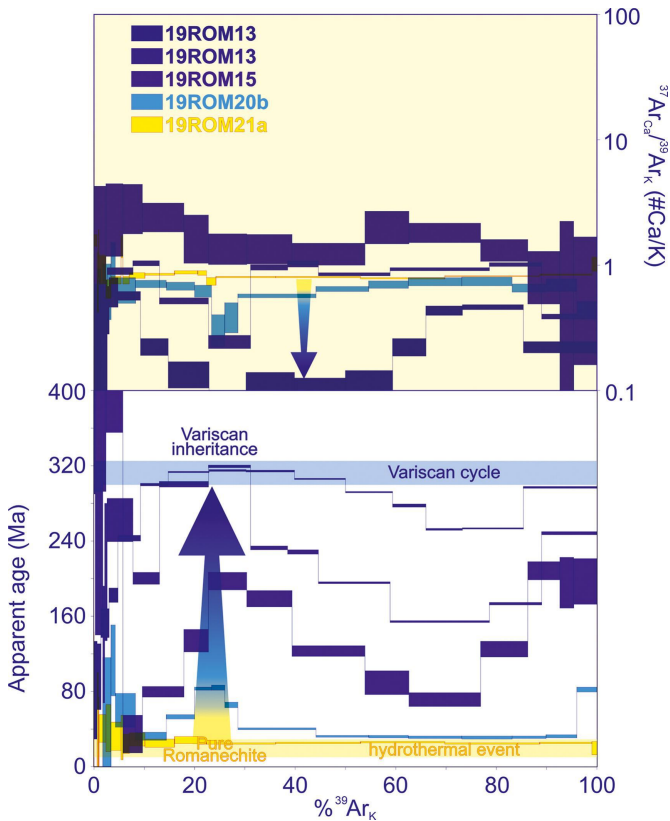


Figure 8

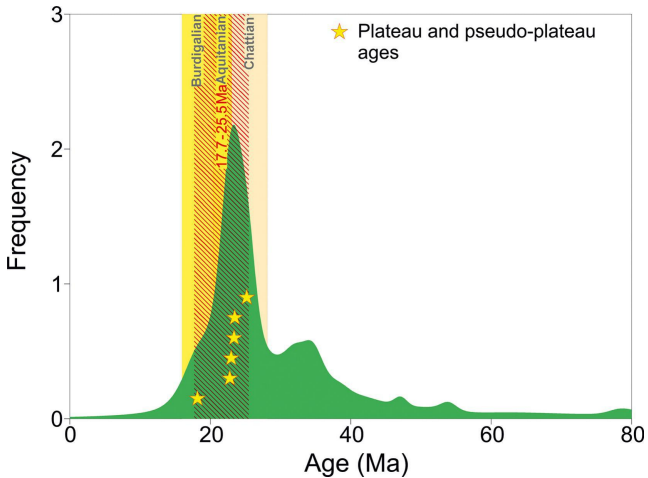


Figure 9

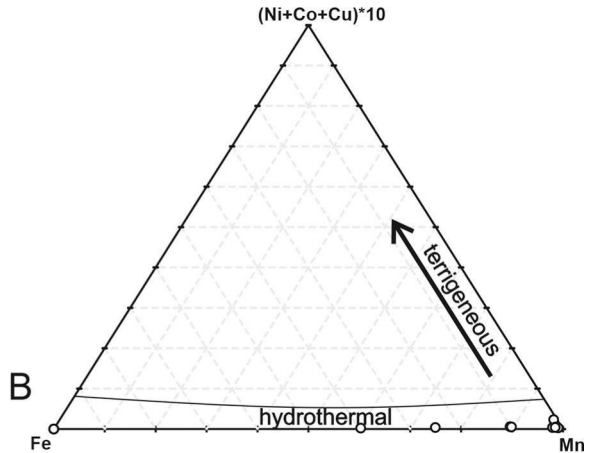
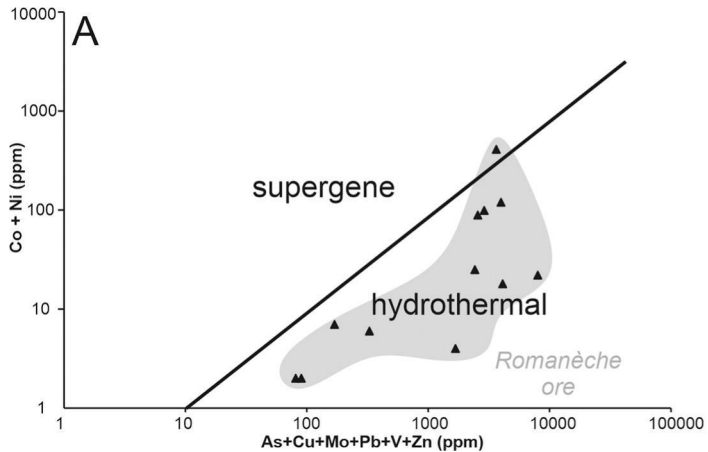


Figure 10